UNIVERSITAT DE BARCELONA

# Spin crossover supramolecular coordination compounds: design, synthesis and properties

Mohanad D .Darawsheh

# Contents

# CHAPTER 1: Introduction

The synthesis and physical properties of coordination compounds and the area of metallo-supramolecular chemistry are of enormous interest to the inorganic chemistry community for their potential in many applications. In this context, two topics from the field of molecular magnetism have been especially relevant; the spin crossover (SCO) phenomenon and single molecular magnet (SMM) behaviour. This introduction will concentrate on the area of SCO since most of the compounds in this thesis exhibit this behavior. However, a brief introduction about SMMs will also be given. Another section will focus on the dinuclear supramolecular helicates and the bis-prazolylpyridine ligands, since these are the main subject of the thesis.

## 1.1 Introduction to Spin Crossover

The spin crossover phenomenon refers to the switching of the spin state of a transition metal ion in a coordination compound due to an external perturbation like temperature, pressure, light irradiation or magnetic field. SCO has been observed in iron(II),[1,2] iron(III),[3–7] cobalt(II)[3,5,7–9] and to less extent, in cobalt(III), chromium(II), manganese(II) and manganese(III).[10–14] The following discussion will focus on Fe(II) systems since it is the subject of this thesis.

In octahedral environment, the *d* orbitals of transition metal ions are split into two subsets of $t_{2g}$ ($d_{xy}$, $d_{yz}$, $d_{zx}$) and $e_g$ ($d_{z^2}$ and $d_{x^2-y^2}$) orbitals where the difference in energy is the ligand field splitting $\Delta$ (Figure 1.1). The magnitude of $\Delta$ relative to the spin pairing energy $P$ of the electrons decides between the two possible spin configurations for $d^4$-$d^7$ transition metal ions. When $\Delta >> P$, the ion will exhibit low spin (LS) state, where the electrons fill first the low-lying orbitals ($t_{2g}$). For $\Delta << P$, the ion will have the same multiplicity as the free ion following Hund's rule and thus will exhibit high spin (HS) configuration (Figure 1.1). When the difference between $\Delta$ and $P$ is very small, a transition between LS and HS may occur as a result of external perturbations.

In the case of iron (II), there are 6 electrons in the *d* orbitals. In an octahedral coordination sphere and in the presence of weak ligand field, the *d* orbitals will split giving a HS $^5T_{2g}$ ground state, as indicated by Tanabe-Sugano diagram (Figure 1.1).

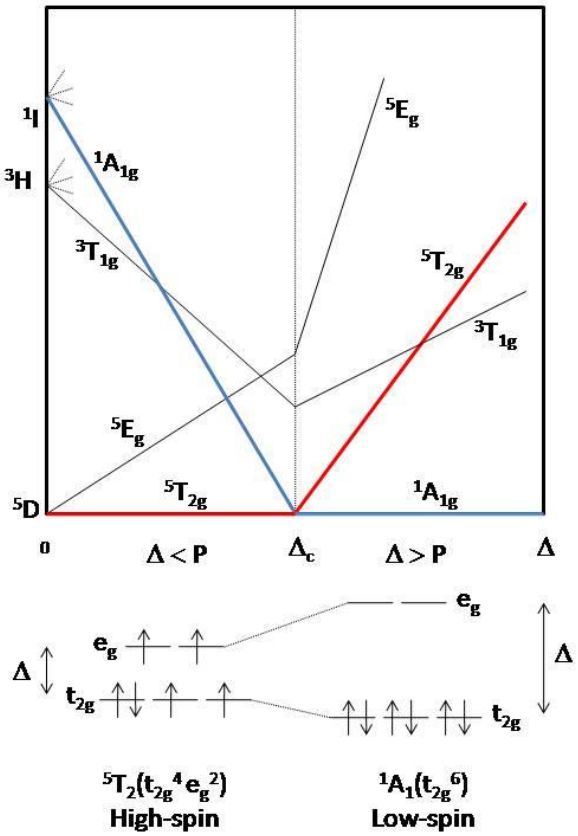


**Figure 1.1**: Simplified Tanabe-Sugano diagram and the electronic configurations of the two possible spin states of a $d^6$ metal ion in octahedral environment. Adapted from reference 15.

This results into a paramagnetic system with $S = 2$. Increasing the ligand field strength above the critical value will favor the LS $^1A_g$ ground state with no unpaired electrons ($S = 0$). When $\Delta$ for a given system is close to the critical value observed in the Tanabe-Sugano diagram (Figure 1.1), a possible transition between $^5T_{2g}$ and $^1A_g$ can occur, thus leading to a SCO behavior. The ligand field strength is determined by the Fe-L distance, in addition to the nature of the donor ligand. The potential energy diagram for the HS and LS states along the totally symmetric stretch vibration is shown in Figure 1.2. The $^5T_{2g}$ (HS) potential well is shifted toward a greater (Fe-L) distance due to the presence of two electrons in antibonding $e_g$ orbitals. In the case of $^1A_g$, all the electrons are in the non-bonding $t_{2g}$ orbitals. The $r_{LS}$ Fe-N distances fall in the range 1.95-2.0 Å whereas the $r_{HS}$ distances are around 0.2 Å longer (i.e. $\Delta r_{HL} = r_{HS}\text{-}r_{LS} \approx 0.2$ Å).[16] The vertical shift of the potential wells depends on the nature of the ligand. When the difference of the zero-point energies for the LS and HS states $E^0_{HL} = E^0_{HS} - E^0_{LS}$ falls in the range of the accessible energy ($K_BT$), thermal population of the HS states may occur at high

temperatures. The transition occurs since the entropy of the HS state is larger due to its higher density of vibrational states.

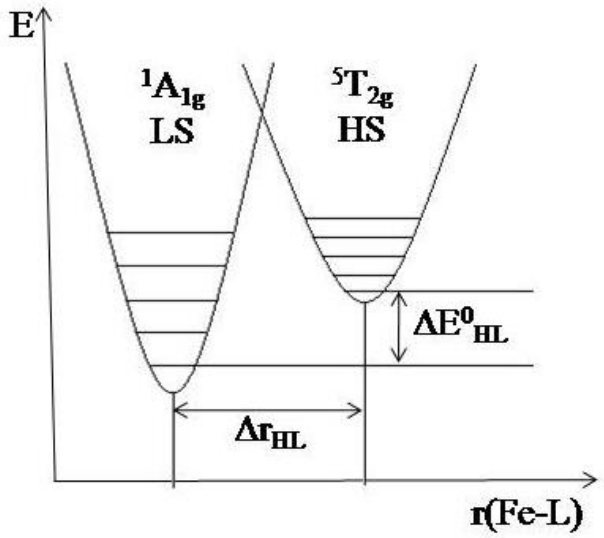


**Figure 1.2**: The potential wells for the HS and LS states along the symmetric metal-ligand stretch vibration (Fe-L) where L is the donor atom. Adapted from reference 17.

The spin transition LS→HS is usually accompanied by changes in spectral, magnetic and structural properties. This allows monitoring the SCO by several measurements such as crystal structure determination, temperature dependence magnetic susceptibility, Mossbauer and vibrational spectroscopy or heat capacity. The thermal spin transition can be represented using $\gamma_{HS}$ (which indicates the mole fraction of Fe(II) centers exhibiting HS state) as a function of temperature. The resulting curves can present different shapes depending on the cooperativity, completeness or the presence of step-wise spin transitions (Figure 1.3). The degree of cooperativity arises from the intermolecular interactions, which mediate the propagation of the structural and electronic changes resulting from the SCO throughout the solid. When these interactions are weak, a gradual transition is observed, occurring over a wide range of temperatures (Figure 1.3a). The limiting case of this behavior is the spin transition in solution, where the Boltzmann distribution of the molecular states is dominating.[18] Sometimes the spin transition does not occur for all metal centers of the system, yielding incomplete SCO where a mixture of HS and LS states is present (Figure 1.3b). An abrupt transition (Figure 1.3c) may occur over a narrow temperature range, which results from high cooperativity between the SCO centers in the solid state. This arises

from the presence of strong intermolecular interaction such as hydrogen bonding and $\pi-\pi$ interactions or from having the metals sites connected via bridging ligands as in coordination polymers. In strongly cooperative systems, a hysteresis may result. The hysteresis arises principally from crystallographic phase transitions associated with the spin transition or from intramolecular structural changes effectively propagated between the SCO molecules.[1] The two step transition (Figure 1.3d) often arise from binuclear systems[19] or when two independent lattice sites,[20] in mononuclear systems are present. In this situation, one center exhibits the spin transition before the other yielding an intermediate state (HS-LS). However, it must be noted that two-step transitions have been observed also in systems where there is only one lattice site.[21]

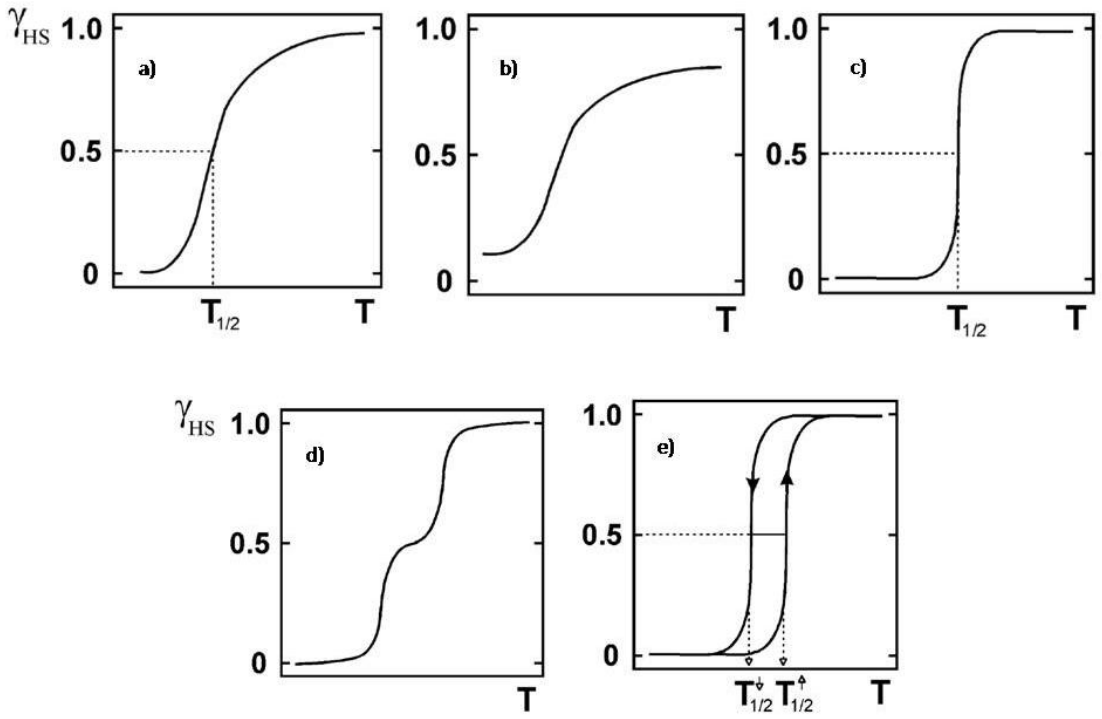


**Figure 1.3**: The main types of spin transition curves represented as high spin mole fraction ($\gamma_{HS}$) *vs.* temperature ($T$). a) gradual, b) incomplete, c) abrupt, d) two-step and e) abrupt with hysteresis. Taken from reference 1.

The change in the distribution of electrons within the *d* orbitals through the spin transition produces changes in magnetic, structural, optical and vibrational properties of these systems. Of the various methods may be used for monitoring the thermal SCO, in this work we will focus on magnetic susceptibility measurements, crystal structure determination and heat capacity measurements.

**Variable temperature magnetic susceptibility measurements**

The main technique used to monitor the spin transition is measuring the magnetic susceptibility as a function of temperature. The different number of unpaired electrons in HS and LS states which for Fe(II) is four and zero, respectively, yield drastic changes to the magnetic susceptibility $\chi(T)$. These measurements are usually conducted using SQUID magnetometers due to their high sensitivity and accuracy.[22] At a given temperature, the $\chi T$ product is determined by the contribution of the $\chi_{HS}$ and $\chi_{LS}$ according to the mole fraction of each ($\chi(T) = \gamma_{HS}\chi_{HS} + \gamma_{LS}\chi_{LS}$). The SCO curves are now widely expressed in the $\chi T$ *vs. T* form due to practical reasons. However, $\gamma_{HS}(T)$ *vs. T* curves are another way to represent the SCO changes when the pure magnetic susceptibility $\chi(T)$ is known for the pure HS and LS states. In solution, Evan's method[23] is used to determine the magnetic susceptibility, which consists on measuring the shift of a diamagnetic reference signal with or without the presence of the paramagnetic solute.

**Crystal structure determinations**

The spin transition is accompanied by structural changes that can be detected by single crystal X-ray structural studies. Variable temperature crystal structure determinations can provide a deep understanding of the SCO process and the precise effect of the molecular interactions and of the other existing species of the lattice on the spin transition process. For Iron (II), the Fe-Donor distance in the HS state (around 2.18 Å) is ca. 10% larger than that in LS state (around 1.96 Å) as a result of the different electronic distributions, more significantly, the number of electrons on $e_g$ antibonding orbitals.[24,25] This change may also produce an increase of cell volume (3-4%) and the cell paramters.[1,26]

The spin transition from LS to HS states produce usually a deformation in the $FeN_6$ octahedral coordinated geometry that can be gauged by the N-Fe-N angles. The distortion parameters $(\Sigma)$ and $(\Theta)$ are used in SCO compounds to indicate the deviation of a metal ion coordination environment from an ideal octahedral symmetry. The $\Sigma$ parameter can be calculated from the formula $\sum_{i=1}^{12} |90 - a_i|$, where $a_i$ are the twelve cis-N-Fe-N angles about the iron center[24,25] (Figure 1.4). A perfect octahedral complex gives $\Sigma = 0$. The $\Theta$ parameter is more specific and indicates the distortion from an

octahedral towards a trigonal prismatic structure ($\Theta = 0$ perfect octahedral). The calculation of $\Theta$ can be done using the formula $\sum_{i=1}^{24} |60 - \theta_i|$, where $\theta_i$ are the 24 unique N-Fe-N angles measured on the projection of two triangular faces of the octahedron along their pseudo-threefold axis (Figure 1.5, right).[25,27] High spin state complexes of a metal ion usually adopt a less regular (ideal) octahedral coordination geometry than their low spin counterparts[25] and therefore they exhibit higher $\Sigma$ and $\Theta$ values.

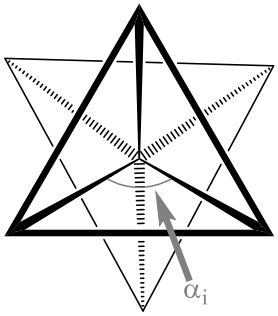


**Figure 1.4**: Definition of the angle $\boldsymbol{\alpha_i}$ used to calculate the distortion parameter $\Sigma$. Adapted from reference 25.

Continuous symmetry measures may be also used to quantify the deviation of the coordination geometry from ideal polihedra. They have been used for example to correlate the change in symmetry and shape of the metal coordination sphere formed by three bidentate ligands on complexes with SCO behaviour.[28] These measures indicate the effect on the trigonal twist angle $\theta$ which is related to the normalized bite (defined as $b=d/r$, where $d$ and $r$ is the donor···donor and the average donor-metal distances, respectively) by the following equation $\theta = 88.0b - 64.9$ (Figure 1.5). The spin transition from LS→HS yield a significant increase in the donor-metal distance without affecting the donor···donor distance. This results a smaller normalized bite and thus a smaller trigonal twist angle $\theta$ which yields a deformation of the octahedral towards trigonal prism.[28] The continuous symmetry measures of $FeN_6$ core can be calculated relative to octahedron $S(O_h)$ or trigonal prism $S(itp)$ geometry.[29–31] The closer to zero is the value for a given ideal symmetry the more ideal is the symmetry of the $FeN_6$ core ($S(O_h) = 0$ ideal octahedron, $S(itp) = 0$ ideal trigonal prism). The HS state exhibits a lager $S(O_h)$ and smaller $S(itp)$ values compared to the LS state, as a result of the associated deformation of the octahedral to trigonal prism.

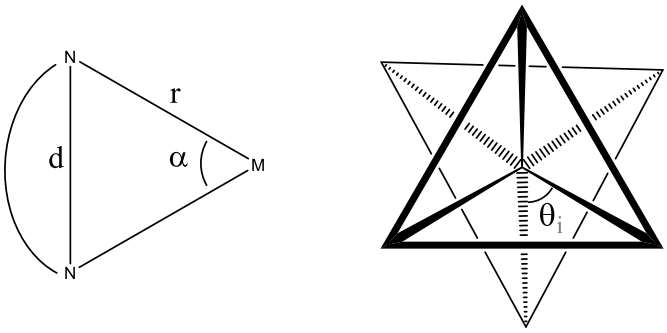


**Figure 1.5**: Definition of the *r* and *d* distances and the trigonal twist angle $\theta$ used in continuous symmetry measures. $\theta_i$ used also to calculate $\Theta$. See text for details. Adapted from reference 28.

## Heat capacity measurements

Differential scanning calorimetry (DSC) can give important information about thermodynamic quantities (entropy and enthalpy) associated to the SCO process, through the measurement of the heat capacity as a function of temperature.[32] Thermal SCO is an entropy-driven process, where usually the entropy difference $\Delta S$ between HS ($^5T_{2g}$) and LS ($^1A_{1g}$) states exceeds the value expected from a purely electronic transition, $\Delta S = R\ ln5 = 13.38$ JK$^{-1}$mol$^{-1}$ in the case of Fe(II), as a result of the changes in the intramolecular vibrations.[1,33] The excess heat capacity $\Delta C_p$ associated with the SCO can be considered as consequence of the phase transition, involving a change in the Gibbs energy of both states. The integration of $\Delta C_p$ with respect to $T$ and $lnT$ gives the changes in enthalpy $\Delta H$ and entropy $\Delta S$ due to the SCO, respectively.[34] The spin transition temperature can be also deduced from these measurements as the maximum of the peak observed in $C_p$ *vs.* $T$ curve.

To investigate the cooperativity of the SCO, Sorai's domain model[32] is commonly used to determine the domain size *n* (number of complexes with spin state conversion in each domain) associated to the SCO process.[35–39] Here, the crystal lattice is considered as a collection of noninteracting domains with uniform size containing *n* complexes. As the number *n* decreases, the heat capacity peak of the SCO process becomes broader and the cooperativity of the transition decreases.[33] Equation 1 can be used to determine the value of *n* by fitting the thermal dependence of $\Delta C_p$.[40]

$$\Delta Cp = \frac{n(\Delta H)^2}{RT^2} \frac{\exp[\frac{n\Delta H}{R}(\frac{1}{T}-\frac{1}{T_{\frac{1}{2}}})]}{(1+\exp[\frac{n\Delta H}{R}(\frac{1}{T}-\frac{1}{T_{\frac{1}{2}}})])^2} \qquad \text{Eq. 1}$$

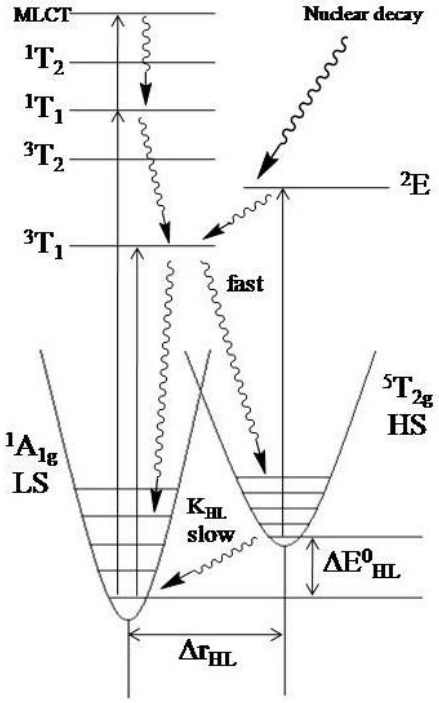


**Figure 1.6**: The electronic structure of Fe(II) SCO complexes illustrating the mechanism of excitation and relaxation in of LIESST and reverse-LIESST mechanisms. Adapted from reference 41.

## 1.2 Light-Induced Excited Spin State Trapping (LIESST) Effect

The Light-Induced Excited Spin State Trapping (LIESST) phenomenon refers to the possibility to convert the stable LS state at low temperatures into a meta-stable HS state using light irradiation (usually green light). This phenomenon was first observed for Fe(II) SCO compounds in solution and solid state by McGarvey et al.[42] and Decurtins et al.[43,44], respectively. Later on, the reverse-LIESST effect could be achieved using red light irradiation to switch the system back the LS state from the meta-stable HS state.[45]

The mechanism of the LIESST and reverse-LIESST effects is illustrated in Figure 1.6. Irradiation the sample in the LS state at low temperature induces the transition to the $^1T_1$ excited state. This short life-time excited state decays rapidly to the $^3T_1$ state which then decays into $^5T_2$ meta-stable state via intersystem crossing. The system remains trapped in this metastable state if the temperature is sufficiently low due to the energy barrier between the HS and the LS states and to the large difference in metal-ligand bond lengths.[41,46] Several techniques may be used to detect the LIESST effect such as infrared, Raman, Mossbauer and optical reflectivity spectroscopies. However, SQUID

magnetometer coupled with an optical source is nowadays widely used for such experiments.[47] The LIESST effect may be characterized by the efficiency of the conversion from the LS state to the meta-stable HS state and by the $T_{LIESST}$ temperature. The latter is defined as the high temperature limit below which the metal-stable HS state persesting[47] and can be obtained from the minimum of the $\partial \chi_M T / \partial T$ *vs. T* curve.

The relaxation kinetics of the meta-stable HS state at low temperature may be interpreted with a nonadiabatic multi-phonon relaxation model.[41] The low temperature quantum tunneling rate $k_{HL}^{0}(T \rightarrow 0)$ of the meta-stable state is governed by the energy gap ($\Delta E_{HL}$) between the lowest vibrational levels of the HS and LS states. As $\Delta E_{HL}$ increases the lifetime of the meta-stable state decreases, which now known as the inverse energy gap law. $\Delta E_{HL}$ increases with increasing ligand field strength which will result into a higher $T_{1/2}$ value. This indicates an inversely proportional relationship between the lifetime of the LIESST meta-stable state and $T_{1/2}$. Moreover, an empirical relationship between the $T_{LIESST}$ temperature and the thermal $T_{1/2}$ temperature was deduced from the investigation a large series of Fe(II) SCO compounds ($T_{LIESST} = T_0 + 0.3T_{1/2}$)[47] where $T_0$ depends on the denticity of the ligand. It was observed that the higher the temperature at which the thermal spin transition occurs the lower the $T_{LIESST}$ is, in agreement with the inverse energy gap law.

## 1.3 SCO in Dinuclear Fe(II) Complexes

Although the majority of Fe(II) SCO complexes are mononuclear or coordination polymer species, there is an increasing interest in discrete polynuclear complexes, of which, dinuclear complexes are the simplest possible framework. Such complexes can provide more combinations of molecular magnetic states (HS-HS, HS-LS and LS-LS, in the case of dinuclear complexes) which can be useful for potential applications in molecular electronics. Moreover, polynuclear complexes give the possibility of combing magnetic properties such as SCO and magnetic coupling interactions[19]. The advantage of discrete polynuclear complexes over polymerics is the ease of crystallization and thus the possibility to establish correlation between structural aspects and the SCO behavior. Designing suitable ligands is the key of the design of useful discrete SCO complexes. The discussion here will focus on the SCO of dinuclear Fe(II) complexes using the designed ligand approach, since it is the subject of this thesis. However, some examples of dinuclear systems using commercial bridging ligands will

be given in the beginning. At a given temperature, a dinuclear complex can exist in HS-HS, HS-LS or LS-LS states. However, the SCO from fully HS to fully LS can occur via one or two-step transitions (i.e [HS-HS]⇔[LS-LS] or [HS-HS]⇔[HS-LS]⇔[LS-LS]). For the two-step spin transition, the enthalpy of the [HS-LS] state must be lower than the average enthalpy of [HS-HS] and [LS-LS] states.[48]

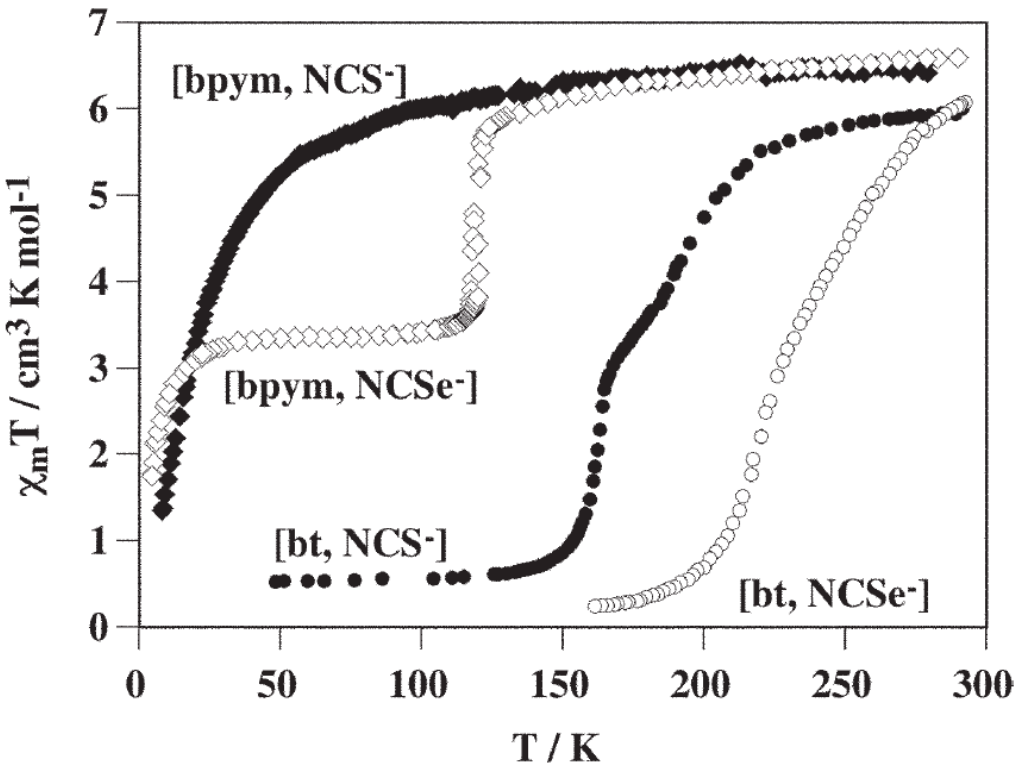


**Figure 1.7**: Thermal dependence of $\chi_M T$ for the dinuclear complexes {[Fe(L)(NCX)$_2$]$_2$(bpym)]} (L=bpym and X=S(bpym, S) or Se (bpym, Se) and L=bt and X=S (bt, S) or Se (bt, Se)). See Figure 1.8 for ligands structures. Taken from reference 49.

The first reported SCO dinuclear complexes contain the bridging 2.2`-bipyrimidine (bpym) ligand (Figure 1.8), and these have been extensively reviewed before.[49,50] For example, a series of compounds {[Fe(L)(NCX)$_2$]$_2$(bpym)}, where L is 2.2`-bipyrimidine (bpym) or 2,2`-bithiazoline (bt) (Figure 1.8) and X is S or Se, were synthesized and their thermal SCO behavior was studied at different pressures.[50] Depending on the type of the end ligands, no SCO, half SCO or two-step SCO transitions were observed (Figure 1.7). The (bpym, NCS$^-$) complex does not show spin crossover (only antiferromangetic coupling at low temperatures), in contrast to (bpym, NCSe$^-$) complex, where 50% of the Fe(II) centers undergo SCO. More interestingly, the (bt, NCS$^-$) and (bt, NCSe$^-$) complexes exhibit two-step SCO with plateaus that correspond to ca. 50 %

of spin conversion. It was unambiguously shown by mean of Mossbauer spectroscopy in an applied magnetic field that the transition from full HS to full LS states occurs via an intermediate state ([HS-HS]→[HS-LS]→[LS-LS]).[51] The shift to higher temperatures of the $T_{1/2}$ when $NCS^-$ is replaced by $NCSe^-$ is due to the increase in the ligand field around the Fe(II) centers. The SCO of these complexes could be tuned by applying different pressures, which affects also the [HS-LS] intermediate state as a result of the change in the intermolecular interactions that stabilize such state.[50,52]

Other commercial bridging ligands used to prepare dinuclear Fe(II) complexes with the help of blocking terminal ligands to complete octahedral coordination are presented in Figure 1.8. These complexes have been recently reviewed by Olguin and Brooker.[19] These authors called these complexes as supramolecular where the dinuclear complex arises from ditopic bridging ligand combined with blocking/terminal ligands. Some of these complexes will be mentioned here briefly. The complex $[Fe_2(phdia)_2(\mu{-}phdia)(NCS)_4]$ (Figure 1.8) exhibits incomplete 2-step SCO from mostly-[HS-HS]→[HS-LS]→[LS-LS] states where the Mossbauer spectroscopy revealed the presence of the localized [HS-LS] state.[53] The complexes $[Fe_2(tpa)_2(\mu{-}H_2bptz)](ClO_4)_4$ and $[Fe_2(phen)_2(\mu{-}bpym)(NCS)_4]$ (Figure 1.8) showed abrupt half-SCO from [HS-HS] to [HS-LS] states centered at 134 and 170 K respectively.[54] Another complex where only 50% of the Fe(II) centers undergo SCO is $[Fe_2(3\text{-}bpp)_2(\mu{-}4,4`bpy)(SCN)_4].MeOH$[55] (Figure 1.8). Two-step SCO ($T_{1/2}(1)$ = 218, $T_{1/2}(2)$ = 191 K) was observed in complex $[Fe_2(dpia)_2(\mu{-}4,4`bpy)(NCS)_4]$ (Figure 1.8), with an inflection point at 204 K. Although the crystal structure at the inflection point revealed a delocalized [HS-LS] state, the zero-field Mossbauer spectroscopy indicated the occurrence of such intermediate state.[56] One-step transition [HS-HS]⇔[LS-LS] was observed on the complex $[Fe_2(Hsaltrz)_5(NCS)_4]\cdot 4MeOH$ (Figure 1.8) centered at 150 K which was proofed by variable temperature crystal structure measurements.[57]

Another approach for preparing dinuclear SCO Fe(II) complexes consists on the designing of ligands with two isolated binding pockets, which was also reviewed by Olguin and Brooker.[19] Only the systems with no interaction between the two well separated Fe(II) metal ions will be discussed here, focusing on the dinuclear helicates since it's the subject of this thesis.

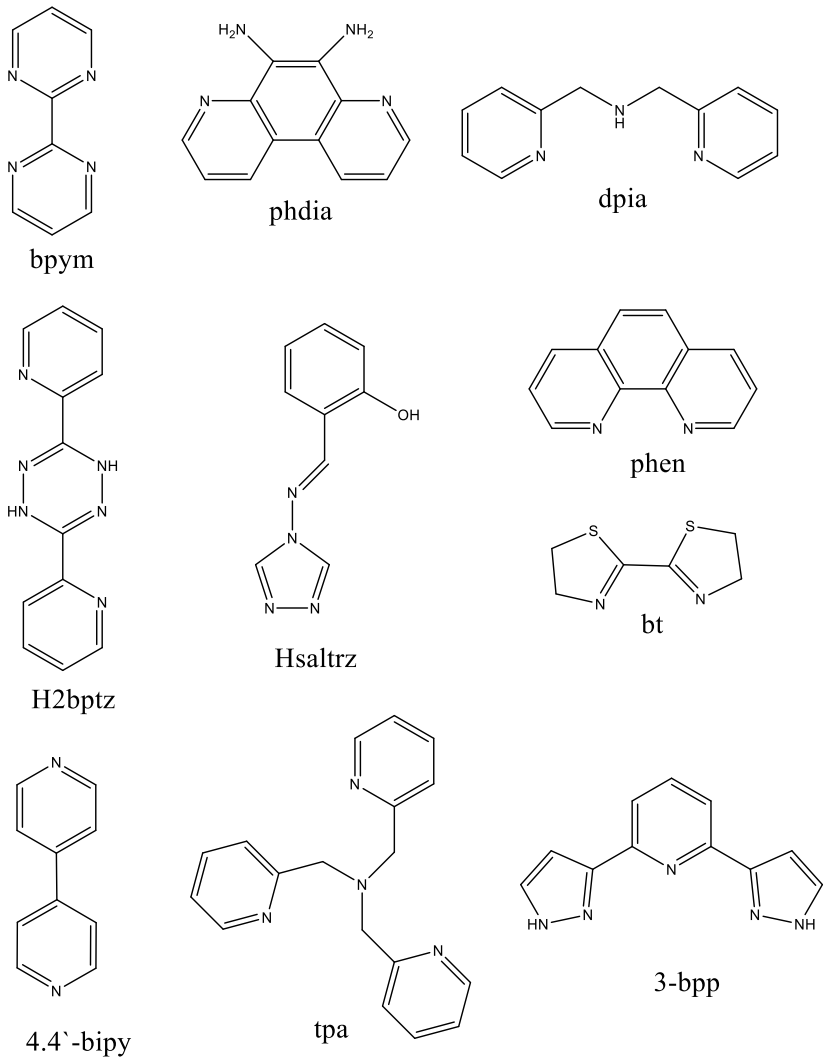


**Figure 1.8**: Bridging and blocking-terminal ligands used to prepare dinuclear SCO Fe(II) compounds.

Complexes $[Fe_2(ddpp)_2(NCS)_4]\cdot nCH_2Cl_2$ (n = 0, 1 or 4) (Figure 1.9) with different solvates were prepared and they showed different SCO behavior.[58] The tetra-$CH_2Cl_2$ solvate undergos a gradual two-step transition ($T_{1/2}(1)$ = 180, $T_{1/2}(2)$ = 80 K), and it is the first example with all the states [HS-HS], [HS-LS] and [LS-LS] structurally characterized. The two iron centers are crystallographically independent at all temperatures. The mono-$CH_2CL_2$ solvate undergoes a gradual one-step SCO centered at 200 K. The desolvated complex does not show any SCO and remains at the [HS-HS] state at all temperatures. The same complexes with $CHCl_3$ as solvate $[Fe_2(ddpp)_2(NCS)_4]\cdot nCHCl_3$(n = 0, 1, 3 or 4) have been also studied. The tetra- and tris-$CHCl_3$ solvates show one-step SCO centered at 148 and 200 K, respectively. Crystal structure measurements revealed only one crystallographically unique Fe(II) center for

tetra-solvate complex at all temperatures in contrast to other solvate complexes. The mono-solvate complex shows only incomplete SCO whereas the desolvated complex remains at the [HS-HS] state without any SCO.

Three dinuclear helicate complexes, $[Fe_2(L^{Im})_3]X_4 \cdot 2H_2O$ (where $L^{Im}$ is a ditopic Schiff base ligand, Figure 1.9, and X = $PF_6^-$, $BF_4^-$ or $ClO_4^-$), were prepared by Tuna et al[59]. The structure consists of three ligands wrapping around two Fe(II) centers making a triple-stranded helicate (Figure 1.10). The complexes exhibit extensive hydrogen bonding of the external imidazole hydrogen atom with solvents and anion molecules. The $PF_6^-$ and $BF_4^-$ complexes exhibit incomplete gradual SCO from [HS-HS] to [LS-LS]. The authors expected that $ClO_4^-$ complex undergos a half-SCO as indicated by the plateau at low temperatures ($\chi_M T = 3.81$ $cm^3Kmol^{-1}$). However, The latter complex was studied again by Garcia et al.[60] using applied magnetic field Mossbauer spectroscopy which showed that half of the iron centers exhibit two-step SCO from [HS-HS] to [LS-LS] states ($T_{1/2}(1) = 240$, $T_{1/2}(2) = 120$ K) while the other half remains in the [HS-HS] state over all the temperatures. This indicates that that the two-step transition occurs via the [HS-LS] intermediate state. The nature of the counterions affects dramatically the SCO behavior of the cationic helicates which not unprecedented for such systems.

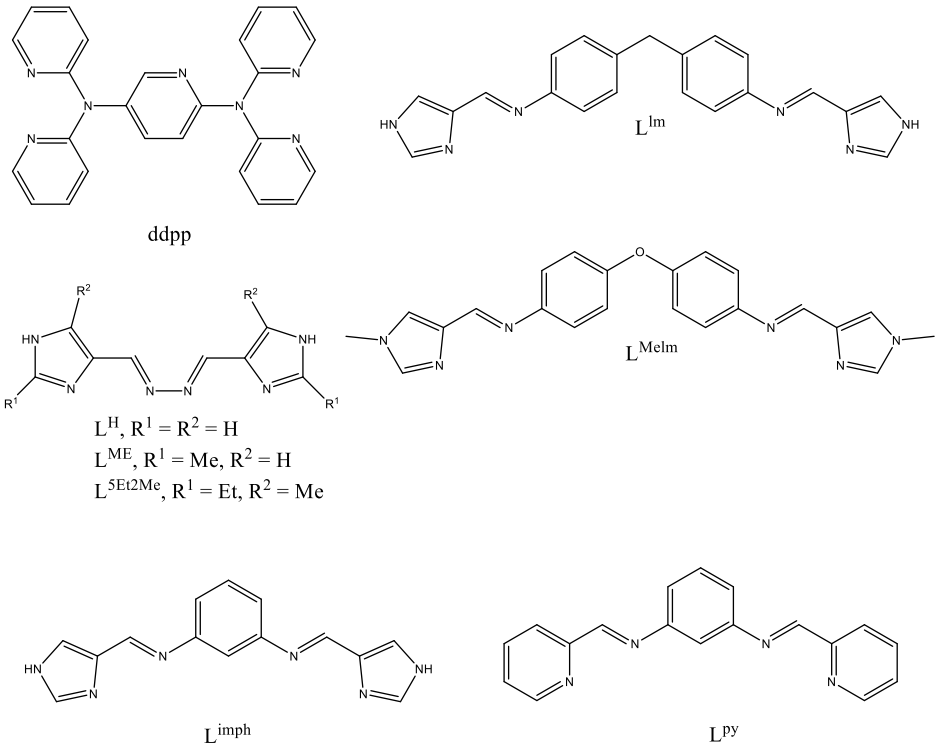


**Figure 1.9**: Designed ligands used to prepare dinuclear Fe(II) complexes.

Recently, similar Schiff bases were used to prepare triple-stranded mesocates[61], namely $Fe_2(L^{imph})_3(BF_4)_4$ and $Fe(L^{py})_3(BF_4)_4$ (Figure 1.9). The imidazole ligand stabilizes the [HS-HS] over all the temperatures, which is explained by the mechanical strain that locks the Fe-N distance in the HS states. The pyridine ligand exhibits [LS-LS] state up to 300 K where gradual SCO starts and only 20 % of metal centers have switched to [HS-HS] states at 400 K.

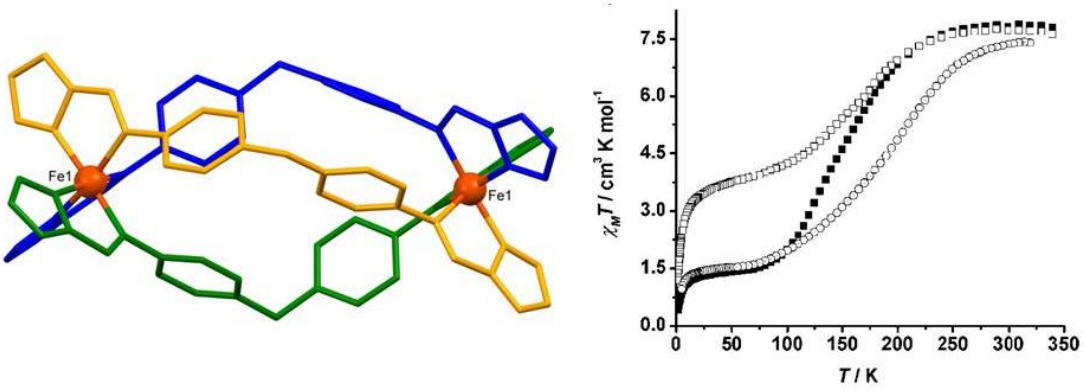


**Figure 1.10**: Molecular representation of the triple-stranded helicate $[Fe_2(L^{Im})_3]^{4+}$. Thermal dependence of $\chi_M T$ for the dinuclear helicate $[Fe_2(L^{Im})_3]X_4 \cdot 2H_2O$ (X = $PF_6^-$ (circles), $BF_4^-$ (filled squares) and $ClO_4^-$ (open squares). SQUID measurements are taken from Reference 59.

Pelleteret et al[62] reported triple-stranded helicate $[Fe_2(L^{MeIm})_3](ClO_4)_4.2MeCN$ where $L^{MeIm}$ is also a bis-bidentate Schiff base ligand (Figures 1.9 and 1.11). The complex exhibits one-step SCO from [HS-HS] to [LS-LS] states upon cooling whereas upon heating very close two-step SCO processes are observed ($T_{1/2}(1)$ = 147, $T_{1/2}(2)$ = 166 K). The water solvate analogue $[Fe_2(L^{MeIm})_3](ClO_4)_4.xH_2O$ exhibits different magnetic properties as a result of the different intermolecular interactions.[63] The complex undergoes only half-SCO from the [HS-HS] to the [HS-LS] states, where the $T_{1/2}$ (in the range 210-265 K) is sensitive to the degree of hydration (x= 1-4) (Figure 1.11).

A series of triple stranded helicates, $[Fe_2(L^R)_3](X)_4$ (R=H or Me, Figure 1.9, X= $ClO_4^-$ or $BF_4^-$), was prepared by Sunatsuki et al.[64] The stronger ligand field provided by adding methyl group in the position 2 of the imidazole ring (Figure 1.9) caused to [LS-LS] state over all the studied temperatures. In contrast, the helicates with $R^1$ = H exhibit half-SCO from [HS-HS] to [HS-LS] centered at 240 K in the case of $ClO_4^-$ complex, which was shown also on crystal structure and by Mossbauer spectroscopy. The $BF_4^-$ analogue was obtained as needle and block shaped polymorphs. The needles exhibit similar SCO to the $ClO_4^-$ complex centered at 254 K. In contrast, the polymorph

obtained as blocks undergoes a more abrupt half-SCO with hysteresis ($T_{1/2}(\uparrow)$ = 190 and $T_{1/2}(\downarrow)$ = 183 K) from [HS-HS] to [HS-LS] states. Interestingly, adding two methyl groups in the 2 and 5 positions of the imidazole rings does not stabilize the [LS-LS] state as expected with increasing the ligand field. Two polymorphs of $[Fe_2(L^{2Et5Me})_3](ClO_4)_4$ were obtained (Figure 1.9) as plate and block crystals. The plates exhibit SCO from [HS-HS] to [LS-LS] states while the blocks remain in the [HS-HS] state.[65]

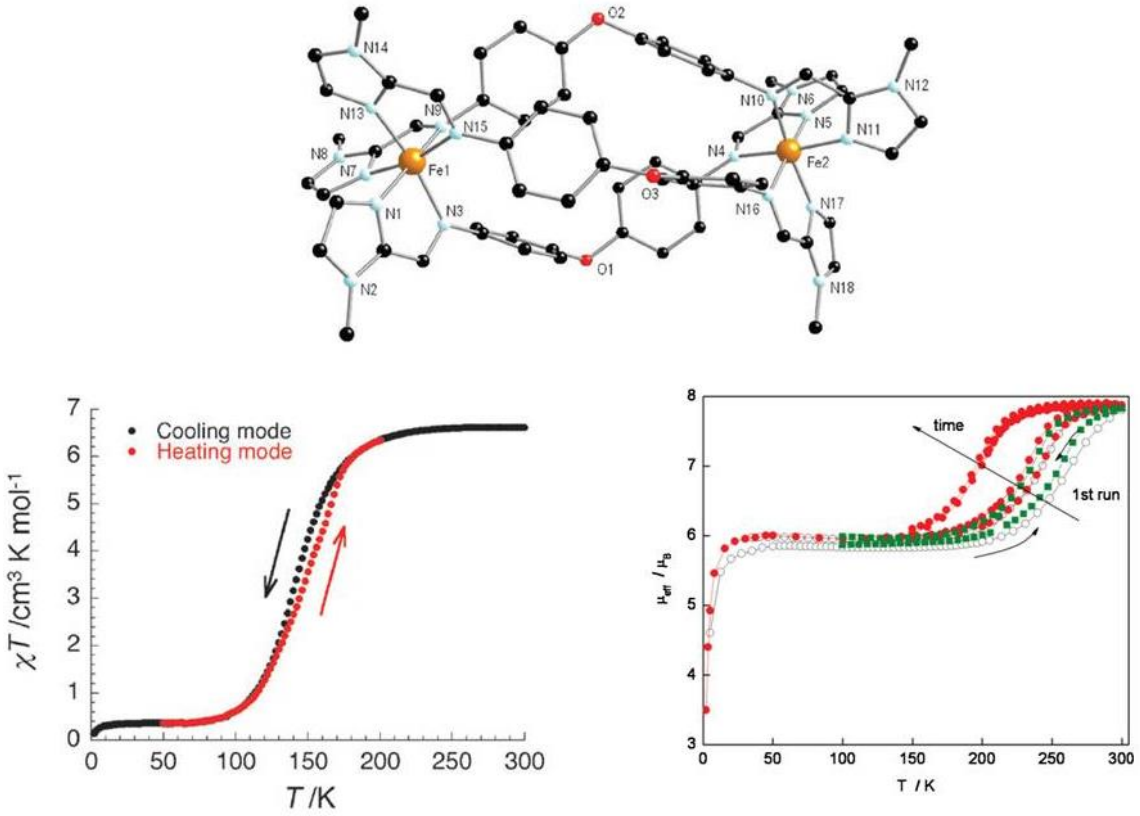


**Figure 1.11**:Top) Molecualr representation of the triple stranded helicate $[Fe_2(L^{MeIm})_3]^{4+}$. Bottom) Thermal dependence of $\chi_M T$ for the dinuclear helicate $[Fe_2(L^{MeIm})_3](ClO_4)_4 \cdot 2MeCN$ (left) and $[Fe_2(L^{MeIm})_3](ClO_4)_4 \cdot xH_2O$ (right). Taken from references 62 and 63.

In all these examples, trapping of the dinuclear complexes in the [HS-LS] state is quite common place perhaps due to the highly constrained ligands and the high number of intermolecular interactions, which eventually stabilize such state and do not allow the transition to the [LS-LS] state.

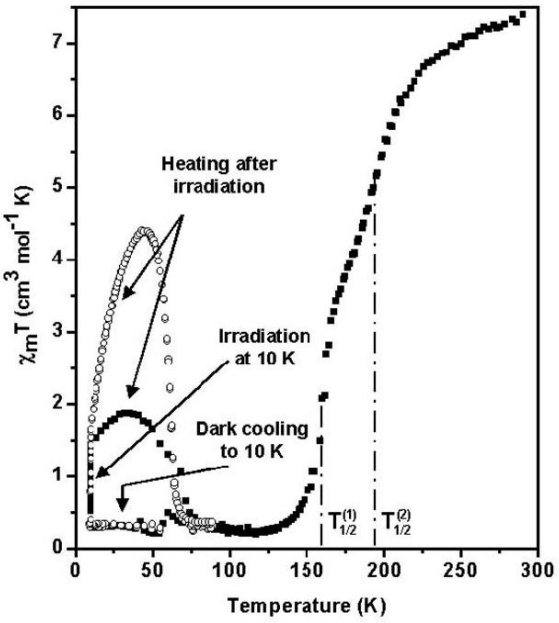


**Figure 1.12**: Thermal dependence of $\chi_M T$ for {[Fe(bt)(NCS)$_2$]$_2$bpym} in the cooling mode and LIESST effect experiment by irradiation with 1342 nm light (closed symbols) and red light (open symbols). Taken from ref 67.

## 1.4 LIESST Effect in Dinuclear Fe(II) Complexes

The first example of the LIESST effect on a dinuclear Fe(II) complex was observed on the compound {[Fe(bt)(NCS)$_2$]$_2$bpym} by Letard et al.[68] (Figures 1.12 and 1.8). The behavior after irradiation in this system is different than observed in mononuclear complexes. Upon irradiating the [LS-LS] ground state using red light, the $\chi_M T$ value increased to 1.6 cm$^3$Kmol$^{-1}$. Upon cooling, this value was decreased to around 0.8 cm$^3$Kmol$^{-1}$. Upon heating in the dark, the $\chi_M T$ value increased significantly to reach a value around 4.6 cm$^3$Kmol$^{-1}$. This behavior was explained by a synergy between the intramolecular antiferromagnetic interactions of the Fe(II) centers in the [HS-HS] state and the LIESST effect. The maximum $\chi_M T$ value at 44 K indicate the recovery of the [HS-HS] state by irradiation while the reduction in $\chi_M T$ value at low temperatures is due to the antiferromagnetic interaction. These results were confirmed by Mossbauer and vibrational spectroscopy.[69] Heating over 45 K yielded a sharp thermal relaxation to the [LS-LS] ground state.

Moreover, selective photo-switching starting from the [LS-LS] state to either a metastable [HS-LS] state or to the [HS-HS] state was observed for

{[Fe(bt)(NCS)$_2$]$_2$bpym}[67] (Figures 1.12 and 1.8). Trapping of the [HS-HS] state by irradiation with red light has been discussed above. However, since two-step SCO was observed for this compound, irradiation with infrared (1343 nm) light could trap the [HS-LS] state. The $\chi_M T$ value increased to 1.5 cm$^3$Kmol$^{-1}$ upon irradiation, and with heating in the dark the $\chi_M T$ value increased slightly further to reach 1.8 cm$^3$Kmol$^{-1}$. This small increase corresponds to the zero field splitting effect for the high spin centers present in the mixed spin state. The presence of the meta stable [HS-LS] state was also confirmed by Raman scattering and x-ray diffraction.[69]

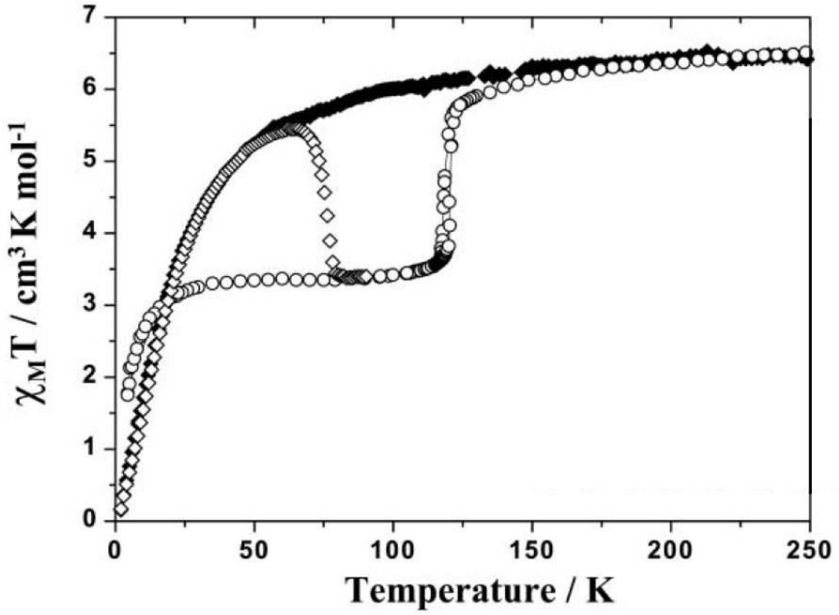


**Figure 1.13**: Thermal dependency of the $\chi_M T$ for (♦) {[Fe(bpym)(NCS)$_2$]$_2$bpym} and (○) {[Fe(bpym)(NCSe)$_2$]$_2$bpym} without irradiation and (◊) *LIESST* effect measurements of the latter. Taken from reference 70.

Another interesting example that illustrate this synergy between the intramolecular interactions and LIESST effect is the compound {[Fe(bpym)(NCSe)$_2$]$_2$bpym} (Figures 1.13 and 1.8), which undergoes half-SCO from the [HS-HS] to the [HS-LS] states.[70] Irradiating this compound with red light at 10 K shows a decrease in the $\chi_M T$ value from 2.6 cm$^3$Kmol$^{-1}$to 1.55 cm$^3$Kmol$^{-1}$. This decrease was observed below 18 K in contrast to the behavior above the same temperature where the $\chi_M T$ increase under light irradiation. This complicated behavior was explained by the presence of intramolecular antiferromagnetic interactions at low temperature between both HS iron centers. Interestingly, below 40 K, the $\chi_M T$ *vs.* $T$ curve of the photo-induced species is identical

to that of {[Fe(bpym)$(NCS)_2]_2$bpym}, which does not exhibit SCO and remains at the [HS-HS] state and only exhibits intramolecular antiferromagnetic interaction. This indicates that LIESST effect on {[Fe(bt)$(NCSe)_2]_2$bpym} yields a metastable [HS-HS]. Heating over 44 K results in the relaxation of the [HS-HS] state to the [HS-LS] ground state.

For dinuclear Fe(II) complexes with well separated metal centers, no intramolecular interaction is expected. Here, the LIESST effect can produce [HS-HS] or [LS-HS] metastable states starting from the [LS-LS] ground state. For the compounds where the [HS-LS] one is the ground state at low temperatures, irradiation with light will produce the [HS-HS] state.

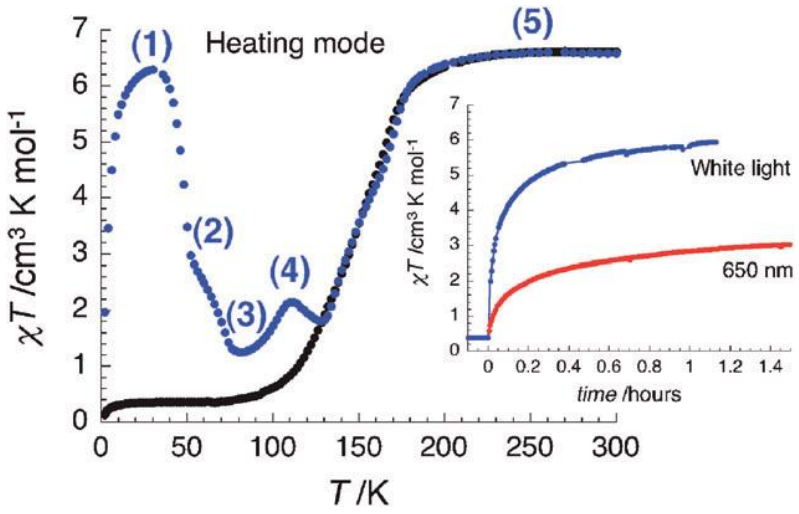


**Figure 1.14**:$\chi_M T$ vs. $T$ plot for $[Fe_2(L^{MeIm})_3](ClO_4)_4 \cdot 2MeCN$ after (blue) and before (black) irradiation with white light. Inset: $\chi_M T$ *vs.* time plot of the same compound under irradiation with white light or 650 nm at 10 K. Taken from reference 62.

Only one example of the LIESST effect on a dinuclear helicate has been reported in the literature. Indeed, irradiation of the dinuclear helicate $[Fe_2(L^{MeIm})_3](ClO_4)_4 \cdot 2MeCN$ resulted in an increase of the $\chi_M T$ value from 0.35 $cm^3Kmol^{-1}$ to 6 $cm^3Kmol^{-1}$ (Figure 1.14). This corresponds to a metastable [HS-HS] state. The thermal relaxation to the [LS-LS] ground state occurs through a complicated sequence of regimes as shown in Figure 1.14. The authors explained this behavior invoking two different relaxation mechanisms associated with the two Fe(II) sites of the dinuclear helicate. They expect that one HS Fe(II) center relax faster than the second one generating a [HS-LS] metastable state. The authors think that the increase in $\chi_M T$ (in step 4, Figure 1.14) is a

signature of some non-thermodynamic metastable dinuclear [LS-HS] species that isothermally converted to [HS-HS] state, which relaxes again at higher temperatures unveiling a third relaxation process.

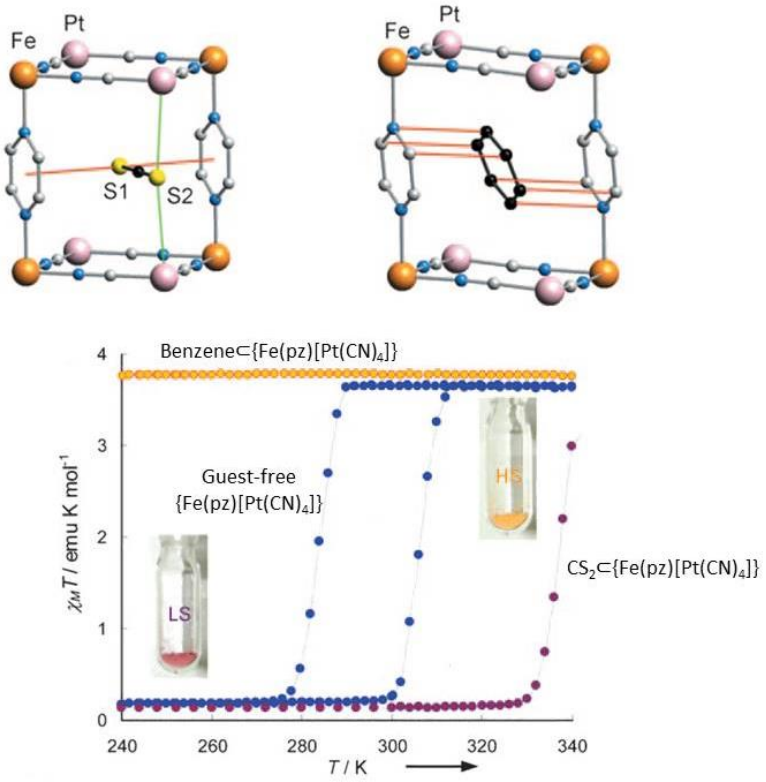


**Figure 1.15**: Top) The basic cavity structure of $CS_2$⊂{Fe(pz)[Pt(CN)$_4$]} (left) Benzene⊂{Fe(pz)[Pt(CN)$_4$]} (right) showing the host-guest interactions. Bottom) the magnetic behavior of the guest-free {Fe(pz)[Pt(CN)$_4$]} coordination polymer and its clathrates. Taken from reference 71.

## 1.5 Guest⊂Host Induced SCO

Porous coordination polymers (PCPs) are amongst the most studied host-guest SCO categories.[72–83] The chemical response of such frameworks are of the root of drastic physico-chemical changes, like the spin state of the Fe(II) centers. A good example of these SCO-PCPs are the Hofmann-type three-dimensional (3*D*) coordination polymers {Fe(pz)[M(CN)$_4$]} (pz = pyrazine, M=Ni(II), Pd(II), Pt(II))[84] which show cooperative thermal and light induced spin transition in the region of room temperature. The guest-free {Fe(pz)[Pt(CN)$_4$]} displays a first order SCO with an approximately 25 K wide hysteresis ($T_{1/2}$(↑) = 309 K, $T_{1/2}$(↓) = 285 K, Figure 1.15).[71] This guest-free framework adsorbs various guest molecules from the gas phase or from solution and forms their

clathrates. The Benzene⊂{Fe(pz)[Pt(CN)$_4$]} clathrate stabilizes the HS state over the temperature range 2-340 K (Figure 1.15). Interestingly, after desorption of benzene under vacuum, the system maintains the HS state at low temperatures over a period of months. In contrast, the $CS_2$⊂{Fe(pz)[Pt(CN)$_4$]}clathrate stabilizes the LS state over the temperature range 2-330 K. Above 330 K, the $\chi_M T$ increases because of the release of $CS_2$ (Figure 1.15). This different guest response is due to varying interactions of each guest with the host framework as illustrated in Figure 1.15, which agree with the theoretical calculations.

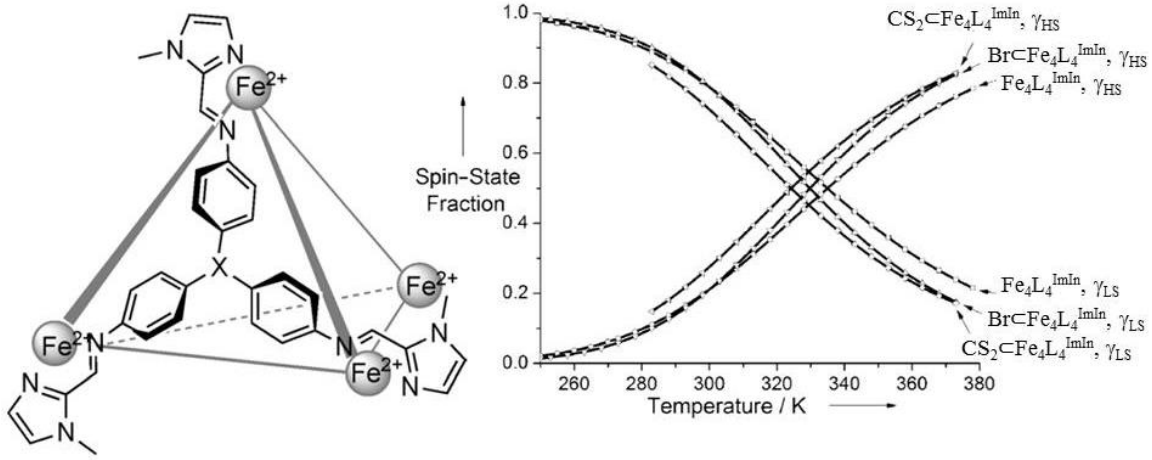


**Figure 1.16**: Left) representation of the tetrahedral capsule $Fe_4L_4^{ImIn}$. Right) HS and LS states fractions for the Fe(II) centers in the guest-free capsule $Fe_4L_4^{ImIn}$, in Br⊂[$Fe_4L_4^{ImIn}$] and in $CS_2$⊂[$Fe_4L_4^{ImIn}$] , as a function of temperature. The data were determined from variable temperature $^1$H NMR experiments in nitromethane. Taken from reference 85.

On the other hand, examples on encapsulated-guest effect on discrete cage are rarely found in the literature. Bilbeisi et al.[85] studied the encapsulated guest effect on the SCO of a [$Fe_4L_4^{ImIn}$](OTf)$_8$ tetrahedral capsule where $L^{ImIn}$ is an imidazolylimine ligand (Figure 1.16). In solid state, the [$Fe_4L_4^{ImIn}$] capsule exhibits the LS state up to 300 K. Higher temperature measurements in the solid state were not possible due to instrumental limitations caused by solvent loss. However, it was possible to study the SCO behavior in nitromethane solution using variable temperature $^1$H NMR spectroscopy. The SCO in the guest-free capsule was observed with $T_{1/2}$ = 333 K and solution thermodynamic parameters of $\Delta H$ = 31.6 ± 0.4 and $\Delta S$ = 94.1 ± 1. For the Br⊂ [Fe4$L_4^{ImIn}$] and the $CS_2$⊂[Fe4$L_4^{ImIn}$] encapsulated systems, the SCO from the LS to the

HS state was shifted to lower temperatures ($T_{1/2}$ = 328 and 324, respectively) in comparison with the guest-free capsule (Figure 1.16). This change in the SCO was explained by the geometrical influences of the guest on the capsule which results in minor changes to the HS/LS state relative energies. Thus, the distribution of the spin state population varies with the size of the guest. The encapsulation of the $CS_2$, a larger guest than the $Br^-$ ion, causes greater geometrical changes, leading to an increase of the HS state population at a given temperature.

## 1.6 Influence of Non-Coordinated Anions and Solvents on the SCO

The SCO depends on the crystal field caused by the ligands, which could be also affected by interactions with non-coordinated ions and solvent molecules via hydrogen bonding, aromatic ring stackings and van der Waals interactions.

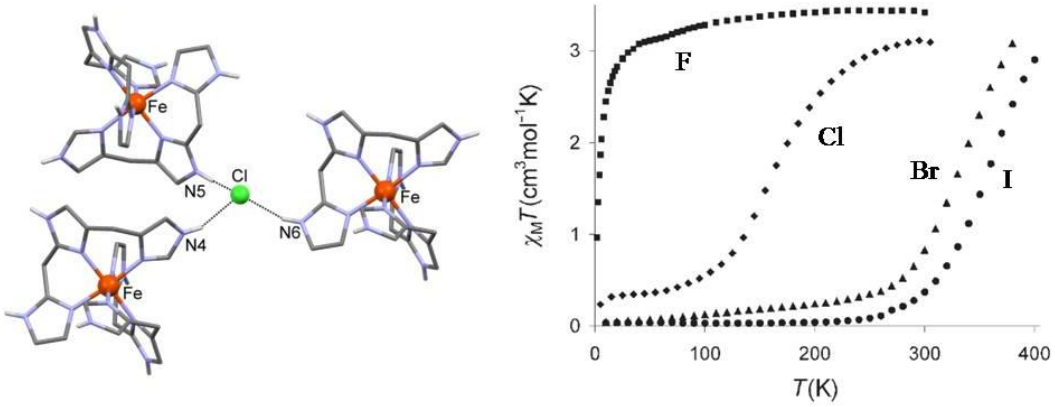


**Figure 1.17**: Left) View of part of hydrogen bond network of the complex $[Fe(trim)_2]Cl_2$. Right) $\chi_M T$ vs. $T$ plot for $[Fe(trim)_2]X_2$ where X = $F^-$, $Cl^-$, $Br^-$ or $I^-$. Taken from reference 86.

Lemercier et al.[86] prepared a series of complexes involving the same $[Fe(trim)_2]^{2+}$ complex cation (Figure 1.17) and varying only the out-of-sphere halide anions, which interacts with the imidazole rings of the ligand via hydrogen bonds. The variety of $T_{1/2}$ values is impressive, spanning from about 179 K for $Cl^-$ to about 380 K for $I^-$ (Figure 1.17). The $F^-$ complex does not exhibit any significant SCO. All the complexes are isostructural, the only significant change being the nature of the halide ion. The differences in the magnetic behavior were explained by the differing inductive effect of the anions, which is transmitted to the donor nitrogen atoms through the hydrogen bonds involving the imidazole rings. The increase of the basicity of the anion and thus the increase of the inductive effect follow the trend $F^->Cl^->Br^->I^-$. The highly basic $F^-$

and $Cl^-$ ions have stronger inductive effect (stronger H···X hydrogen bond) which results in the weakening of the Fe-N bonds and thus stabilizes the HS state. The increase of $T_{1/2}$ follows the trend $I^->Br^->Cl^->F^-$ which agrees with above explanation. These results have been supported with the theoretical calculations.

Interactions with non-coordinated solvents can also affect the SCO behavior in dramatic ways. One of the best examples of such effect is the series of compounds $[Fe(2\text{-}pic)_3]Cl_2 \cdot solv$ (solv = EtOH, MeOH, $H_2O$, $2H_2O$).[87] These compounds were studied by means of Mossbauer spectroscopy in order to investigate the effect of the solvents on the SCO. The dehydrate sample does not exhibit SCO while the monohydrate sample shows SCO with a wide hysteresis ($T_{1/2}(\uparrow)$ = 290 K, $T_{1/2}(\downarrow)$ = 200 K, Figure 1.18). On the other hand, the methanolated complex shows only gradual SCO around 160 K. Slightly changing the solvate to ethanol, the complex exhibits a more steep transition around 120 K (Figure 1.18). The different hydrogen bonding interactions between the solvents and the cation are the reason of such a large change in the SCO behavior. This shows how the SCO is sensitive to any slight change in the lattice.

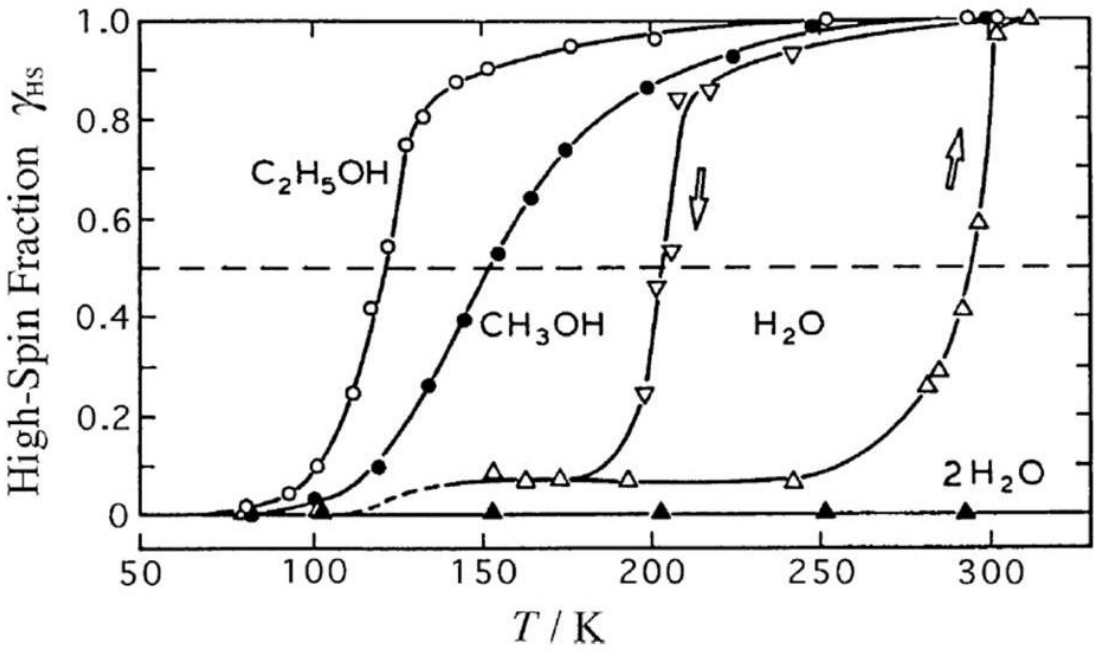


**Figure 1.18**: $\gamma_{HS}$ vs $T$ curves for the different solvates of the compound $[Fe(2\text{-}pic)_3]Cl_2$.Solv (Solv = EtOH, MeOH, $H_2O$, $2H_2O$). Taken from reference 2.

## 1.7 Brief Introduction to Single Moecular Magnets (SMMs)

Single molecule magnets SMMs are molecular species that display characteristic properties of bulk magnetic materials. SMMs can be magnetized by an applied magnetic field and then retain their magnetization after removal this field for an appreciable time below a certain temperature.[88] This slow relaxation of the magnetization is the most fascinating aspect of SMMs and could be of the root of future applications in information storage. The key factor of such compounds is that each molecule in SMM compounds exhibits slow-relaxation of the magnetization and thus behaves as a molecular nanomagnet.

In SMMs, the magnetic behavior is governed by the anisotropy (zero-field splitting) parameters (*D* and *E*) of the spin ground state, which can be written according to the following Hamiltonian $\widehat{H} = DS_z^2 + E\left(S_x^2 - S_y^2\right)$, where *D* and *E* are the axial and rhombic ZFS parameters, respectively. Although most SMMs exhibit a negative *D* value, it is known now that compounds with positive *D* value can also exhibit SMM behavior.[89–93]

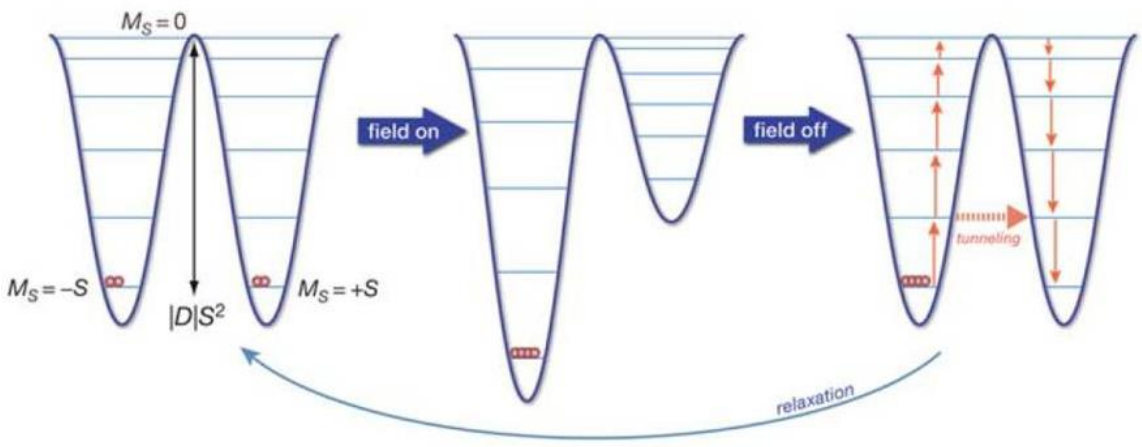


**Figure 1.19**: Sketch diagram of the double-well and the demonstrating of the magnetization and magnetic relaxation processes in a SMM. Taken from reference 88.

The process of slow relaxation of the magnetization in SMMs can be better illustrated using the double-well energy diagram (Figure 1.19). The opposite signs of ± $M_S$ states are plotted in different wells. When there is no external magnetic field, all the levels with equal $|M_S|$ are degenerated. Application of an external magnetic field parallel to the magnetization axis, yields stabilization of $-M_S$ levels and destabilization of $+M_S$ levels.

When the saturation occurs, only the $M_S$ = -$S$ level is populated. When the field is removed, the system returns to thermal equilibrium through a series of steps. This relaxation process depends on the value of the energy barrier $U_{eff}$ which slows it down. The barrier arises from the uniaxial magnetic anisotropy $D$ of the spin ground state, according to the expression $U_{eff} = |D|S^2$($U_{eff} = |D|S^2$-*1/4*, for half-integer spin). The larger the energy barrier is, the longer will be the relaxation. An important manifestation of this barrier is a magnetic hysteresis of molecular origin, which was first observed for the compound $Mn_{12}O_{12}(CH_3CO_2)_{16}(H_2O)_4$.[94] There are two specific characteristics for SMM that have been described very well; frequency dependence of the imaginary part of the magnetic susceptibility under an *ac* magnetic field and the presence of steps in the hysteresis loops due to tunneling effects. The frequency dependence of the imaginary component of the susceptibility is usually employed to diagnose the SMM behavior, because in many cases it is technically difficult to characterize the hysteresis steps.[95]

The majority of SMM compounds are multinuclear transition metal clusters with a large $S$ value. However, theoretical studies showed that the magnitude of $D$ decreases with increasing $S$, implying that the search of new SMMs with large $U_{eff}$ should not be pursued solely in terms of maximizing $S$.[88] Recently, a subclass of SMMs emerged a side from this group, namely single ion magnets SIMs where only one paramagnetic center with large $D$ values is the responsible of the SMM-like behavior. The SIM behavior was first observed on lanthanide ions.[96] However, there are now many examples of *3d* SIMs including Mn(III), Fe(I), Fe(II) and Co(II) based complexes. The latter have been recently reviewed by Craig and Murrie.[97] In chapter 5, we will describe the first example of a SIM based on the $[Cr(oxalate)_3]^{3-}$ metal complex, which is encapsulated inside the cavity of triple stranded helicates.

## 1.8 Metallosupramolecular Chemistry: Triple-Stranded Helicates

The field of metallo-supramolecular chemistry refers generally to the coordination chemistry that studies the molecular structures which interact through non-covalent bonds, such as metal coordination, hydrogen bonding, $\pi$–$\pi$ and van der Waals interactions, electrostatic forces and other weak interactions.[98] This chemistry branch is inspired by Nature and the biological systems, like proteins and enzymes, which depend mainly on such kind of interactions for their functionality. Molecular self-assembly is a

key concept in such chemistry, where the formation of a thermodynamically favored product is guided by means of favored intermolecular interactions.[98]

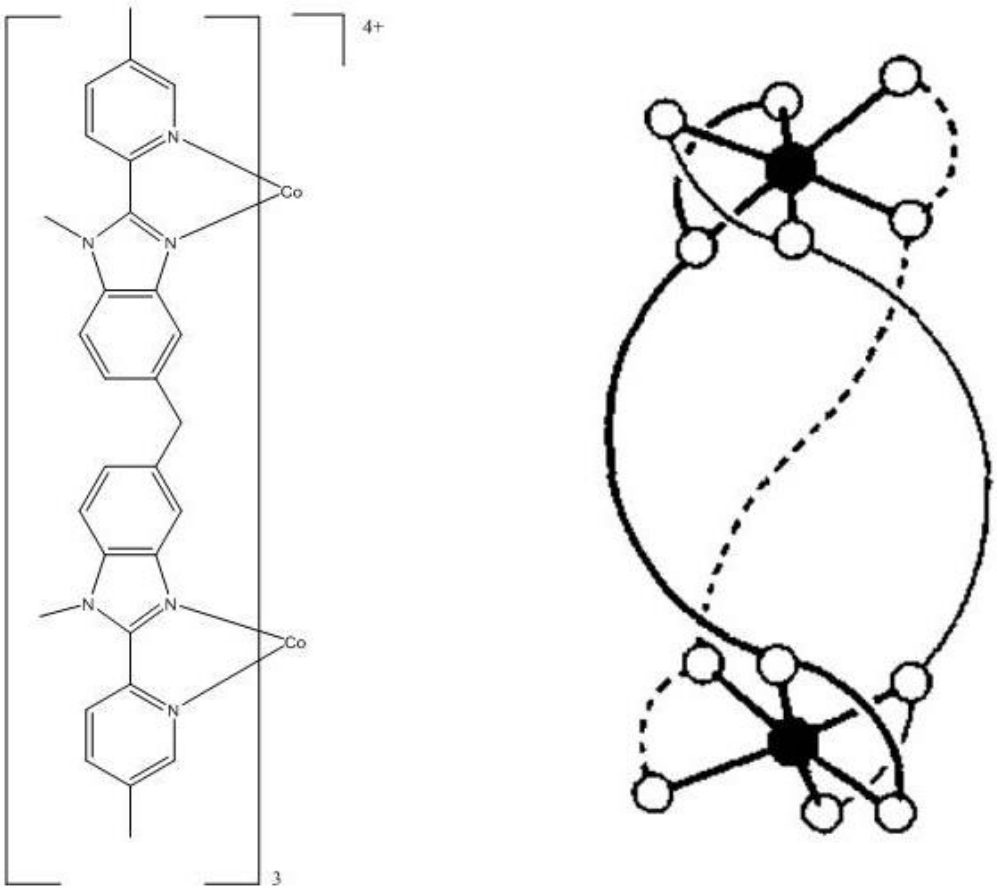


**Figure 1.20**: The first introduced dinuclear triple-stranded helicates formed from ditopic pyridyl-benzimidazole ligand. The helical structure is taken from reference 99.

Helicates are among the metallo-supramolecular compounds where one or more ligand strands wrap around one or more metal ions.[100] Helicates may be single or multiple stranded and may vary in pitch, which is the distance along the helical axis for the strands to complete a full turn.[101] There are several ways to class helicates,[101] which can depend on the number of strands, yielding double-, triple- or quadruple-stranded helicate. When the ligand strands are identical, the helicate is called homostranded whereas in the opposite case, it is called heterostranded helicate. Homotopic strands are those with the same binding pocket type along the length of the ligand. Strands with different binding pockets called heterotopic. In heterotopic stranded helicates, the orientation of the ligands can be head-to-head or heat-to-tail. The most common helicates are homostranded and contain homotopic ligands.

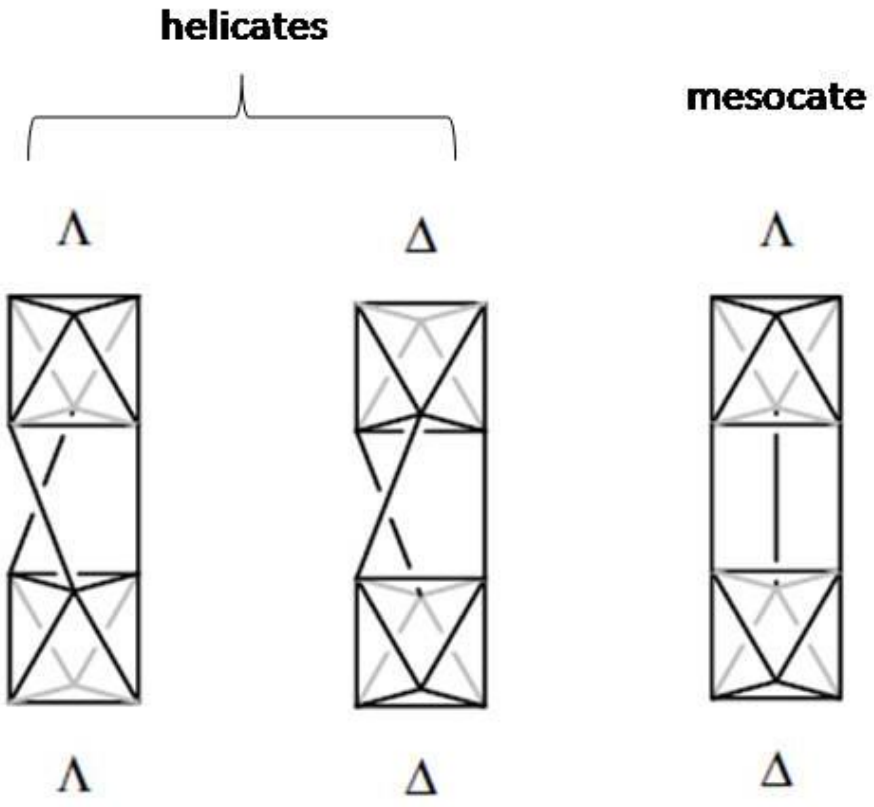


**Figure 1.21**: Illustration of the stereochemistry of both metal ions in dinuclear helicates or mesocates.

Triple stranded helicates among the most common helicates. In them, three ligands wrap around one or more metal ions and they will constitute the focus of the discussion. The number of ligand strands able to coordinate to a given metal ion depends on the favored coordination number of the metal and the denticity of the ligand. For six coordinate metal ions, bidentate ligands will form triple stranded helicates. For polynuclear helicates, a suitable linker or spacer between one or more sites of coordination should be available. The spacer must exhibit a balance between rigidity and flexibility in order to favor the helical twisting around the metal ions. The dinuclear helicates is the simplest possible polynuclear helicate, where only a ditopic ligand is needed. The first example of a dinuclear triple stranded helicate was introduced by Williams et al.[99] using a ditopic bidentate pyridyl-benzimidazole ligand (Figure 1.20). In this structure, the Co(II) ion adopts an octahedral geometry and the ligands wrap around the axis connecting both metals in a helical fashion.

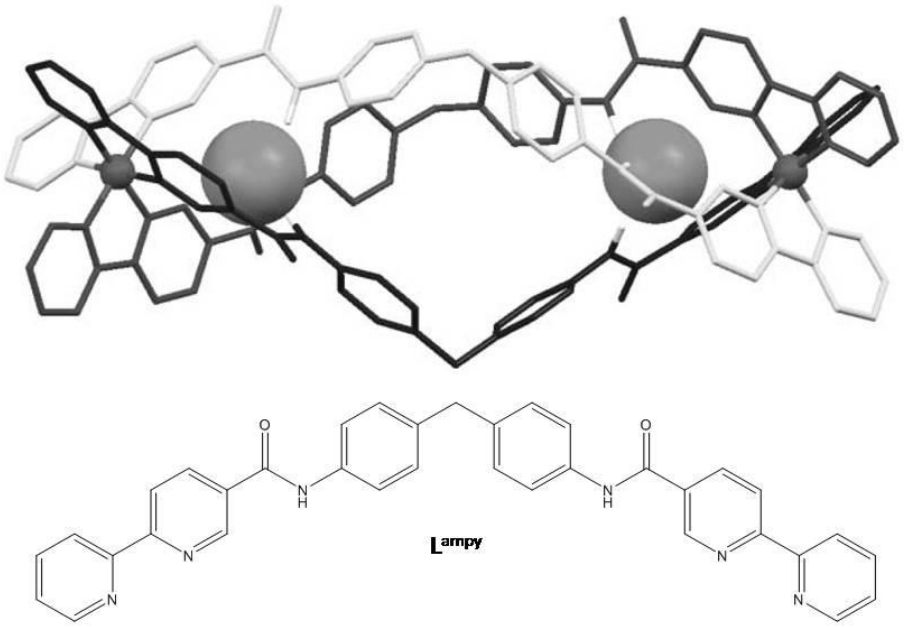


**Figure 1.22**: Molecular model of the triple stranded helicate $[Fe_2(L^{ampy})_3Cl_2]^{2+}$ where two chloride ions are encapsulated inside the cavity, stabilized by the hydrogen bonding with N-H groups. The molecular model is taken from reference 102.

In order to form a helical structure, the stereochemistry around both metal ions must be the same (left handed $\Lambda$, or right handed $\Delta$ configurations). Otherwise, the term mesocate is used for systems with opposite configuration around the metal ions (Figure 1.21). In mesocate, the ligands are not quite wrapping around the metal axis. Usually a racemic mixture of both possible configurations is found within the lattice (i.e. $\Lambda\Lambda$ and $\Delta\Delta$ in the case of dinuclear helicates) (Figure 1.21) except in some cases of stereoselectivity where one of the configurations is favored (such as using achiral ligand).

There are many examples of triple-stranded helicates, and this has been reviewed many times.[100,101,103–105] Moreover, since helicates contain a cavity surrounded by the ligand strands, some of them serve as host for small species, thus yielding interesting host-guest systems. Goeta and Kruger[102] studied the helicate and mesocate formation of a series of new bis-amino-2,2`-bipyridine ligands in solution. Although these complexes exist in both forms (mesocate and helicate) in DMSO solution, addition of $Cl^-$ ions stabilizes the triple stranded helicate, and this was explained by the encapsulation of these ions inside the helical cavity in the ratio 2:1 (Cl:helicate) (Figure 1.22). This encapsulation is stabilized by the hydrogen bonding of the $Cl^-$ ions with the NH groups

of the ligands that are directed to the interior of the cavity (Figure 1.22). This encapsulation was proofed by means of $^{1}H$ NMR and Mass spectrometry.

An interesting study in the formation of helicates or mesocates depending on the nature of the encapsulated ion was carried out by Cui et al.[106] Using a positive charged ligand ($L^{bipy}$, see Figure 1.23), a series of triple stranded helicates and mesocates using Fe(II) and Cu(II) metal ions was prepared. The triple-stranded cages that encapsulate relatively big tetrahedral anions such as $ClO_4^-$, $SO_4^-$ and $BF_4^-$ exhibited a mesocate configuration. On the other hand, the cages that encapsulate relatively small anions such as spherical $Br^-$ or $NO_3^-$ trigonal planar anions exhibit the helicate configuration around the metal ions. This illustrates how sensitive the configuration around the metal ions is to the guest encapsulation. Other earlier examples on helicates as a host species and the template effect of the encapsulated anions can be found in a review by Abrecht.[104]

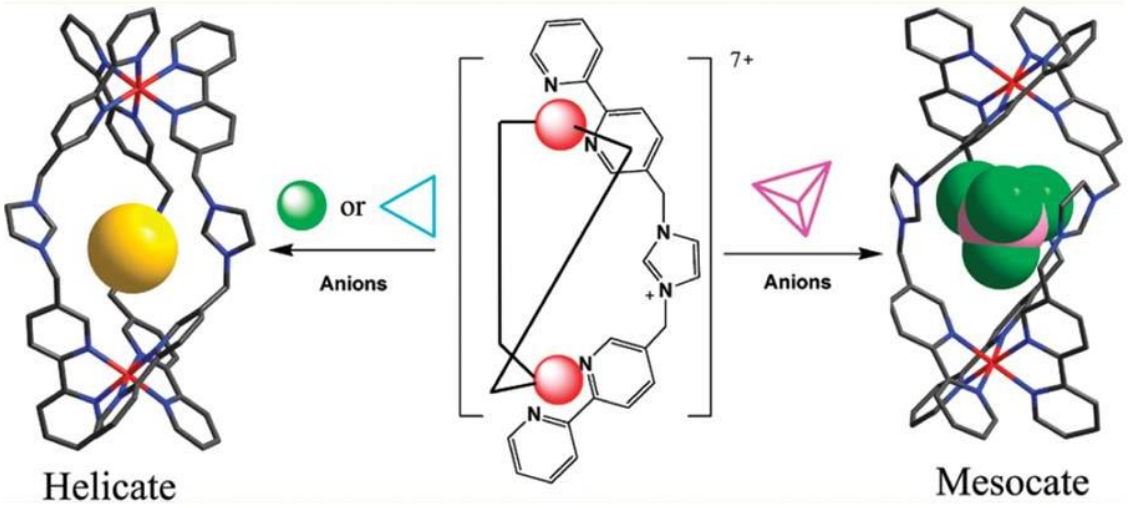


**Figure 1.23**: The formation of triple-stranded helicates or mesocate based on bis-bipyridine ligands ($L^{bipy}$) depending on the type and the size of the encapsulate anions. Taken from reference 106.

One of the applications of some dinuclear helicates stems from their DNA binding ability. The shape and the size of such helicates can sometimes closely mimic the dimensions of protein DNA recognition motifs. Hannon research group was involved in a novel study of DNA binding using a tetracationic triple-stranded helicate based on a bis(pyridylimine) ligand[107] (Figure 1.24).

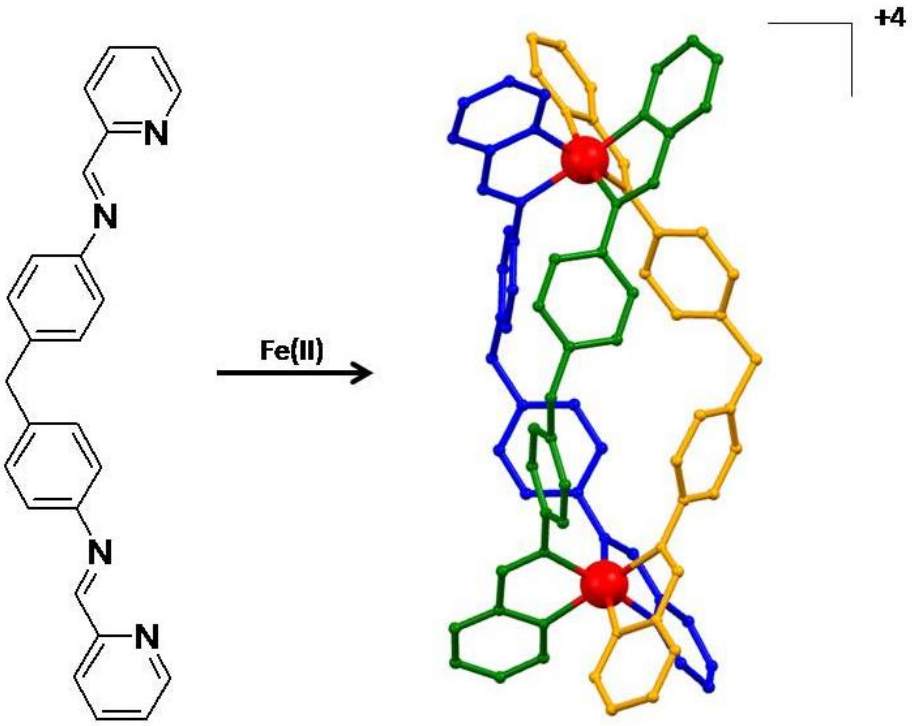


**Figure 1.24**: Design of triple-stranded helicate with potential DNA binding ability. Reproduced from reference 107.

This helicate binds into the major groove of DNA and causes intramolecular DNA coiling.[108] Precise size and shape are the most important factors for such activity more than the charge of the helicate. The helicate was found to induce the formation of a three-way junction of deoxyribonucleotides with the helicate located in the center of the junction.[109] The helicate drug does not suffer any significant conformational change upon binding to DNA. The helicate features two important characteristics that help with such binding; the positive charge that is attracted by the negative charge of the DNA, and large hydrophobic groups (the aromatic groups) that interact through extensive $\pi$-stacking with the thymine and adenine bases at the junction.[110]

## 1.9 Bis-Pyrazolylpyridine Ligands

Through this thesis, two new bis-pyrazolyl-pyridine ligands have been used to prepare novel triple stranded helicates. Other bis-pyrazolyl-pyridine ligands have been used before to prepare helicates and other high nuclear cages. Figure 1.25 illustrates some of these ligands with different types of spacers and linkers. The ligand $L^{m\text{-}py\text{-}H}$ (Figure 1.25) consists of three pyridine groups linked by two pyrazole moieties and forming one

tridentate and two bidentate binding sites. This ligand was used to prepare a heptanuclear helical complex $[Co^{II}_5Fe^{III}_2(L^{m\text{-}py\text{-}H})_6O_6(H_2O)_6](BF_4)_4$ (Figure 1.26).[111] The complex has a helical structure consisting of six ligand units, two Fe(III) ions and five Co(II) ions ions. The helicate here has a core structure in which three Co(II) centers form a planar triangular arrangement and are capped above and below the plane by two $[Fe(III)O_3(H_2O)_3]^{3-}$ units from which each oxo ligand acts as a bridge between the

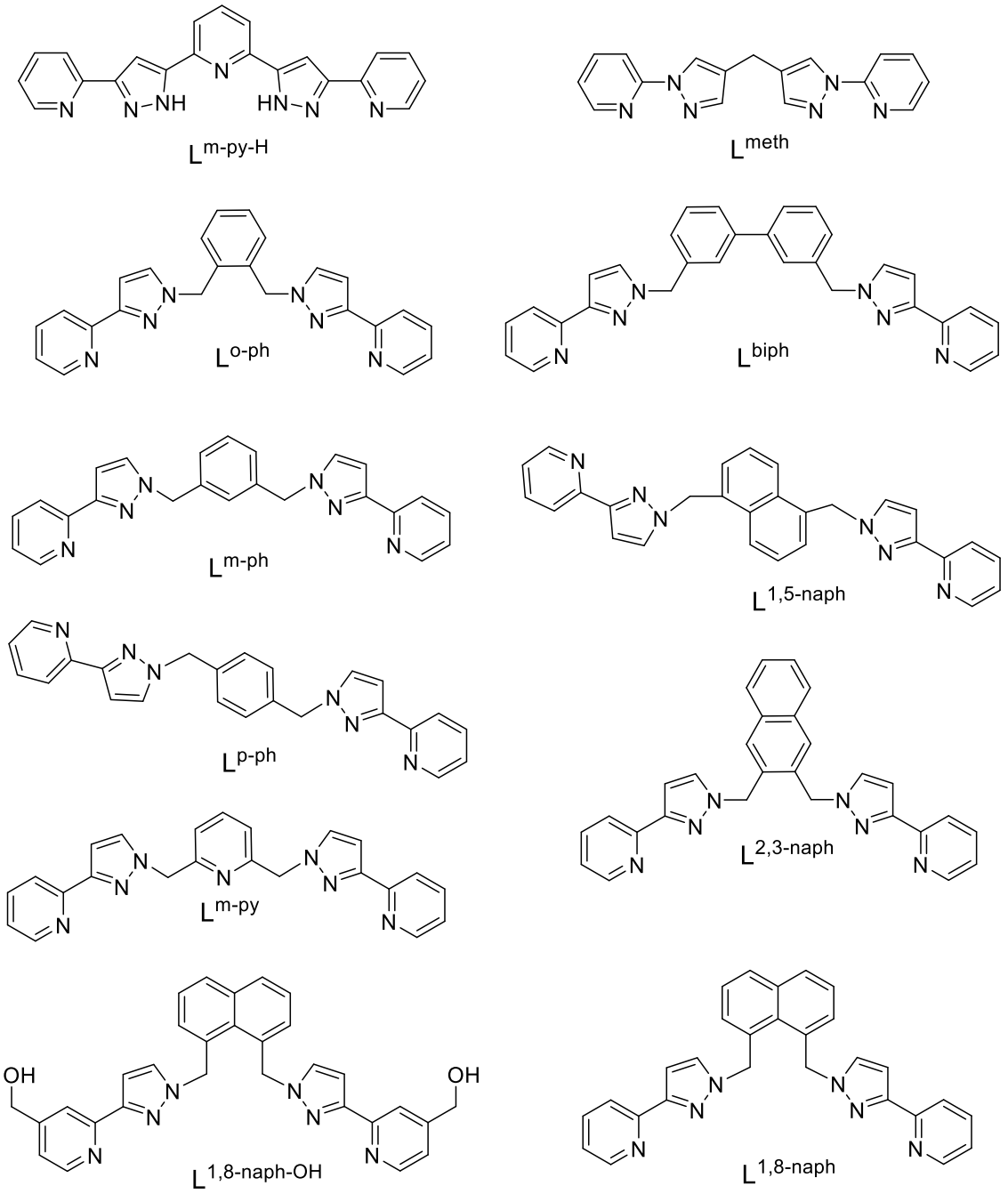


**Figure 1.25**: Bis-pyrazolyl-pyridine ligands used to prepare supramolecular polynuclear cages.

Fe(III) and three Co(II) ions. The oxo core is capped by two distant Co(II) ions located at the ends of the helical clusters, which have $CoN_6$ coordination environment. The three central Co(II) ions have $CoN_4O_2$ coordination environments and are coordinated by two bidentate ligand binding sites and two oxide ions. The same ligand was used to prepare multinuclear iron complexes, [$Fe_5$], [$Fe_7$] and [$Fe_{17}$]. All these complexes have triple stranded helicates structures with pseudo threefold symmetry.[112]

The ligand $L^{meth}$ (Figure 1.25) has been used to prepare dinuclear Fe(II) triple-stranded helicates[113]. The $[Fe_2(L^{meth})_3](BF_4)_4$ helicate was isolated in the solid state and consists of three ligands wrapping around both metals in a helical fashion. $^1$H NMR and UV-vis studies indicate the presence of mostly triple-stranded helicate in solution.

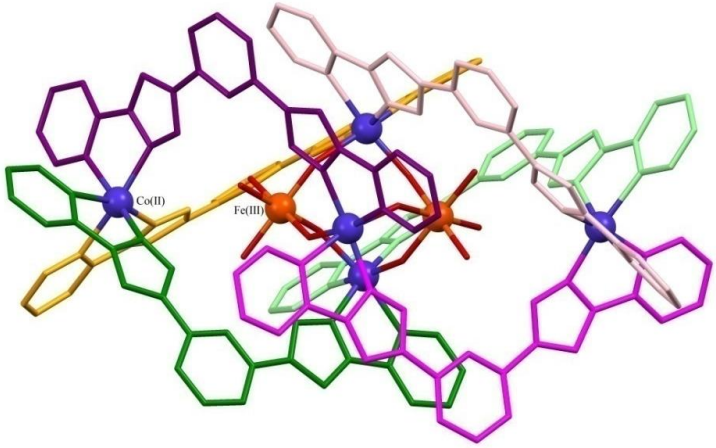


**Figure 1.26**: The helical structures $[Co^{II}_5Fe^{III}_2(L^{m\text{-}py\text{-}H})_6O_6(H_2O)_6]^{4-}$. The six $L^{m\text{-}py\text{-}H}$ ligands are in different colors and oxygen in red. Reproduced from reference 111.

The rest of the pyrazolyl-pyridine ligands in Figure 1.25 are parts of the novel work of Ward research group. These ligands have been used to prepare different molecular cages with metal to ligand ratio 2:3. These cages include $M_2L_3$ triple-stranded mesocates, $M_4L_6$ tetrahedral cages, $M_8L_{12}$ cubic cages and larger $M_{12}L_{18}$ and $M_{16}L_{24}$ cages. Large type cages are not the subject of this thesis and for the interested reader, these have been reviewed by Ward himself.[114]

Ligand $L^{1,8\text{-}naph\text{-}OH}$ (Figure 1.25) was used to prepare triple stranded mesocate with cobalt(II) ions.[115] The structure consists of a triple stranded complex $Co_2(L^{1,8\text{-}naph\text{-}OH})_3$ where three ligands span both metal centers. Within each molecule, the two metal centers have opposite chirality, which indicates the lack of a helical structure (Figure 1.21). The complex has 3-fold rotational symmetry with the $C_3$ axis passing through

both metal centers. In contrast to helicates, mesocate ligands lack 2-fold symmetry, therefore the molecular symmetry is $C_3$ and not $D_3$ as in helicates.

## 1.10 Aim and Scope of the Thesis

The aim of this thesis is the use of supramolecular chemistry tools to tune the SCO properties of dinuclear compounds. Host-guest chemistry is of much interest especially in discrete cages like dinuclear triple-stranded helicates. The nature of the anions and solvent guests can play a major role in the nature of the SCO of such dinuclear Fe(II) metal complexes. Another interesting aspect will be the encapsulation of metal complexes inside the cavity of another discrete metal complex. This can furnish bifunctional host-guest systems. The design of the corresponding ligands is the first stage in such supramolecular chemistry program. A bis-bidentate ligand is needed to prepare a dinuclear triple-stranded helicate, whereas the $FeN_6$ environment is needed to generate SCO behavior of the Fe(II) centers. Thus, bis-prazolyl-pyridine ligand with suitable spacer is a good a candidate of such purpose. The additional N-H group of the pyrazole ring can arise to interesting host-guest chemistry by encapsulate hydrogen acceptor anions.

Chapter 2 introduces two novel bis-pyrazolyl-pyridine ligands used through this thesis and the use of these ligands to prepare host-guest dinuclear triple stranded helicates. Chapter 3 contains the SCO behavior of dineclear triple-stranded helicates with encapsulated halide ions. The SCO can be tuned by the nature of the anions or the solvents to give three stable [HS-HS], [HS-LS] and [LS-LS] states. At low temperature, the metastable [HS-HS] and [HS-LS] states can be recovered via LIESST effect. Chapter 4 introduces a novel dimerized triple stranded mononuclear helicate. The ligand is the same as in chapter 3, but the change in the synthesis procedure yielded different supramolecular chemistry. In these dimers, one side of the bis-pyrazole-pyridine ligands does not participate in coordination bond and remain free. The dimerization occurs via hydrogen bond with the halide anions and the N-H group of the ligands. Chapter 5 contains a novel triple stranded helicates that encapsulate $[M(III)(ox)_3]^{3-}$ (M = Fe and Cr; ox = oxalate) inside their cavity. This yields to bifunctional system where the host exhibits SCO and LIESST effect and the guest exhibits single molecular magnet SMM-like behavior. Finally, chapter 6 contains a magneto-structural correlations for the compounds in this thesis and similar compounds in the literature.

## 1.11 References


1 P. Gütlich and H. A. Goodwin, *Top. Curr. Chem.*, 2004, **233**, 1–47.

2 P. Gütlich, A. B. Gaspar and Y. Garcia, *Beilstein J. Org. Chem.*, 2013, **9**, 342–391.

3 K. S. Murray, *Eur. J. Inorg. Chem.*, 2008, **2008**, 3101–3121.

4 S. V. Larionov, *Russ. J. Coord. Chem.*, 2008, **34**, 237–250.

5 H.-J. Krüger, *Coord. Chem. Rev.*, 2009, **253**, 2450–2459.

6 B. Weber and E.-G. Jäger, *Eur. J. Inorg. Chem.*, 2009, **2009**, 465–477.

7 M. A. Halcrow, *Spin-crossover materials: properties and applications*, John Wiley & Sons, 2013.

8 H. A. Goodwin, *Top. Curr. Chem.*, 2004, **234**, 23–47.

9 S. Hayami, Y. Komatsu, T. Shimizu, H. Kamihata and Y. H. Lee, *Coord. Chem. Rev.*, 2011, **255**, 1981–1990.

10 Y. Garcia and P. Gütlich, *Top. Curr. Chem.*, 2004, **234**, 49–62.

11 G. G. Morgan, K. D. Murnaghan, H. Müller-Bunz, V. McKee and C. J. Harding, *Angew. Chemie - Int. Ed.*, 2006, **45**, 7192–7195.

12 P. N. Martinho, B. Gildea, M. M. Harris, T. Lemma, A. D. Naik, H. M??ller-Bunz, T. E. Keyes, Y. Garcia and G. G. Morgan, *Angew. Chemie - Int. Ed.*, 2012, **51**, 12597–12601.

13 A. J. Fitzpatrick, E. Trzop, H. Müller-Bunz, M. M. Dîrtu, Y. Garcia, E. Collet and G. G. Morgan, *Chem. Commun.*, 2015, **1404709**, 17540–17543.

14 K. Pandurangan, B. Gildea, C. Murray, C. J. Harding, H. Müller-Bunz and G. G. Morgan, *Chem. - A Eur. J.*, 2012, **18**, 2021–2029.

15 J. A. Real, A. B. Gaspar and M. C. Muñoz, *Dalton Trans.*, 2005, 2062–2079.

16 A. Hauser, *Top. Curr. Chem.*, 2004, **233**, 49–58.

17 A. Hauser, *Top. Curr. Chem.*, 2004, **233**, 49–58.

18 M. P. Shores, C. M. Klug and S. R. Fiedler, in *Spin-Crossover Materials: Properties and Applications*, ed. M. A. Halcrow, John Wiley & Sons, 2013, pp. 281–301.

19 J. Olguín and S. Brooker, in *Spin-Crossover Materials: Properties and Applications*, ed. M. A. Halcrow, John Wiley & Sons, 2013, pp. 77–120.

20 G. S. Matouzenko, J.-F. Letard, S. Lecoeq, A. Bousseksou, L. Capes, L. Salmon, M. Perrin, O. Kahn and A. Collet, *Eur. J. Inorg. Chem.*, 2001, 2935–2945.

21 H. Köppen, E. W. Müller, C. P. Köhler, H. Spiering, E. Meissner and P. Gütlich, *Chem. Phys. Lett.*, 1982, **91**, 348–352.

22 R. L. Fagaly, *Rev. Sci. Instrum.*, 2006, **77**, 101101.

23 D. F. Evans, *J. Chem. Soc.*, 1959, 2003–2005.

24 P. Guionneau, M. Marchivie, G. Bravic, J.-F. Létard and D. Chasseau, *Top. Curr.*

*Chem.*, 2004, **234**, 97–128.

25 M. A. Halcrow, *Chem. Soc. Rev.*, 2011, **40**, 4119–4142.

26 E. König, *Struct. Bond.*, 1991, **76**, 51–152.

27 M. Marchivie, P. Guionneau, J. F. Létard and D. Chasseau, *Acta Crystallogr. Sect. B Struct. Sci.*, 2005, **61**, 25–28.

28 S. Alvarez, *J. Am. Chem. Soc.*, 2003, **125**, 6795–6802.

29 The measurments was done using the webpage Http://www.csm.huji.ac.il/new/?cmd=shape.26, or the program SHAPE 2.1.

30 S. Alvarez, D. Avnir, M. Llunell and M. Pinsky, *New J. Chem.*, 2002, **26**, 996–1009.

31 H. Zabrodsky, S. Peleg and D. Avnir, *J. Am. Chem. Soc.*, 1992, **114**, 7843–7851.

32 M. Sorai, M. Nakano and Y. Miyazaki, *Chem. Rev.*, 2006, **106**, 976–1031.

33 M. Sorai, *Top. Curr. Chem.*, 2004, **235**, 153–170.

34 A. Singh and K. N. Shrivastava, *Phys. Status Solidi*, 1979, **95**, 273–277.

35 Z. Arcís-Castillo, L. Piñeiro-López, M. C. Muñoz, R. Ballesteros, B. Abarca and J. A. Real, *CrystEngComm*, 2013, **15**, 3455.

36 N. Wannarit, O. Roubeau, S. Youngme, S. J. Teat and P. Gamez, *Dalt. Trans.*, 2013, **42**, 7120–7130.

37 Z. Yan, J. Y. Li, T. Liu, Z. P. Ni, Y. C. Chen, F. S. Guo and M. L. Tong, *Inorg. Chem.*, 2014, **53**, 8129–8135.

38 N. Wannarit, N. Nassirinia, S. Amani and N. Masciocchi, *Inorg. Chem.*, 2014, **53**, 9827–9836.

39 H. L. C. Feltham, C. Johnson, A. B. S. Elliott, K. C. Gordon, M. Albrecht and S. Brooker, *Inorg. Chem.*, 2015, **54**, 2902–2909.

40 T. Nakamoto, Z. C. Tan and M. Sorai, *Inorg. Chem.*, 2001, **40**, 3805–9.

41 A. Hauser, *Top. Curr. Chem.*, 2004, **234**, 155–198.

42 J. J. McGravey and I. Lawthers, *J. Chem. Soc., Chem. Commun.*, 1982, 906–907.

43 S. Decurtins, P. Gütlich, C. P. Köhler, H. Spiering and A. Hauser, *Chem. Phys. Lett.*, 1984, **105**, 1–4.

44 S. Decurtins, P. Gutlich, K. M. Hasselbach, A. Hauser and H. Spiering, *Inorg. Chem.*, 1985, **24**, 2174–2178.

45 A. Hauser, *Chem. Phys. Lett.*, 1986, **124**, 543–548.

46 G. Létard, Jean-François chastanet, P. Guionneau and C. Desplanches, in *Spin-Crossover Materials: Properties and Applications*, ed. M. A. Halcrow, John Wiley & Sons, 2013, pp. 475–506.

47 J.-F. Létard, *J. Mater. Chem.*, 2006, **16**, 2550.

48 S. Zein and S. A. Borshch, *J. Am. Chem. Soc.*, 2005, **127**, 16197–16201.

49 A. B. Gaspar, M. C. Munoz and J. A. Real, *J. Mater. Chem.*, 2006, **16**, 2522–2533.

50 J. A. Real, A. B. Gaspar, M. C. Muñoz, P. Gütlich, V. Ksenofontov and H. Spiering, *Top. Curr. Chem.*, 2004, **233**, 167–193.

51 V. Ksenofontov, H. Spiering, S. Reiman, Y. Garcia and a B. Gaspar, *Chem. Phys. Lett.*, 2001, **348**, 381–386.

52 V. Ksenofontov, A. B. Gaspar, J. A. Real and P. Gütlich, *J. Phys. Chem. B*, 2001, **105**, 12266–12271.

53 V. Ksenofontov, A. B. Gaspar, V. Niel, S. Reiman, J. a Real and P. Gütlich, *Chemistry*, 2004, **10**, 1291–1298.

54 S. R. Batten, S. R. Batten, J. Bjernemose, J. Bjernemose, P. Jensen, P. Jensen, B. a Leita, B. a Leita, K. S. Murray, K. S. Murray, B. Moubaraki, B. Moubaraki, J. P. Smith, J. P. Smith, H. Toftlund and H. Toftlund, *Society*, 2004, 3370–3375.

55 D. Fedaoui, Y. Bouhadja, A. Kaiba, P. Guionneau, J. F. Létard and P. Rosa, *Eur. J. Inorg. Chem.*, 2008, 1022–1026.

56 A. Y. Verat, N. Ould-Moussa, E. Jeanneau, B. Le Guennic, A. Bousseksou, S. A. Borshch and G. S. Matouzenko, *Chem. - A Eur. J.*, 2009, **15**, 10070–10082.

57 Y. Garcia, F. Robert, A. D. Naik, G. Zhou, B. Tinant, K. Robeyns, S. Michotte and L. Piraux, *J. Am. Chem. Soc.*, 2011, **133**, 15850–15853.

58 J. J. M. Amoore, C. J. Kepert, J. D. Cashion, B. Moubaraki, S. M. Neville and K. S. Murray, *Chem. - A Eur. J.*, 2006, **12**, 8220–8227.

59 F. Tuna, M. R. Lees, G. J. Clarkson and M. J. Hannon, *Chem. - A Eur. J.*, 2004, **10**, 5737–5750.

60 Y. Garcia, C. M. Grunert, S. Reiman, O. Van Campenhoudt and P. Gütlich, *Eur. J. Inorg. Chem.*, 2006, 3333–3339.

61 N. Struch, J. G. Brandenburg, G. Schnakenburg, N. Wagner, J. Beck, S. Grimme and A. L??tzen, *Eur. J. Inorg. Chem.*, 2015, **2015**, 5503–5510.

62 D. Pelleteret, R. Clerac, C. Mathoniere, E. Harte, W. Schmitt and P. E. Kruger, *Chem Commun*, 2009, 221–223.

63 J. A. Thomas, *Dalt. Trans.*, 2011, **40**, 12005.

64 Y. Sunatsuki, R. Kawamoto, K. Fujita, H. Maruyama, T. Suzuki, H. Ishida, M. Kojima, S. Iijima and N. Matsumoto, *Coord. Chem. Rev.*, 2010, **254**, 1871–1881.

65 Y. Sunatsuki, H. Maruyama, K. Fujita, T. Suzuki, M. Kojima and N. Matsumoto, *Bull. Chem. Soc. Jpn.*, 2009, **82**, 1497–1505.

66 R. J. Archer, C. S. Hawes, G. N. L. Jameson, V. McKee, B. Moubaraki, N. F. Chilton, K. S. Murray, W. Schmitt and P. E. Kruger, *Dalton Trans.*, 2011, **40**, 12368–73.

67 N. O. Moussa, G. Molnár, S. Bonhommeau, A. Zwick, S. Mouri, K. Tanaka, J. A. Real and A. Bousseksou, *Phys. Rev. Lett.*, 2005, **94**, 1–4.

68 J. F. Létard, J. A. Real, N. Moliner, A. B. Gaspar, L. Capes, O. Cador and O. Kahn, *J. Am. Chem. Soc.*, 1999, **121**, 10630–10631.

69 A. Bousseksou, G. Molnár, J. A. Real and K. Tanaka, *Coord. Chem. Rev.*, 2007, **251**, 1822–1833.

70 G. Chastanet, C. Carbonera, C. Mingotaud and J.-F. Letard, *J. Mater. Chem.*, 2004, **14**, 3516–3523.

71 M. Ohba, K. Yoneda, G. Agusti, M. C. Muñoz, A. B. Gaspar, J. A. Real, M. Yamasaki, H. Ando, Y. Nakao, S. Sakaki and S. Kitagawa, *Angew. Chemie - Int. Ed.*, 2009, **48**, 4767–4771.

72 J. Y. Li, Y. C. Chen, Z. M. Zhang, W. Liu, Z. P. Ni and M. L. Tong, *Chem. - A Eur. J.*, 2015, **21**, 1645–1651.

73 J.-Y. Li, C.-T. He, Y.-C. Chen, Z.-M. Zhang, W. Liu, Z.-P. Ni and M.-L. Tong, *J. Mater. Chem. C*, 2015, **3**, 7830–7835.

74 M. C. Muñoz and J. A. Real, *Coord. Chem. Rev.*, 2011, **255**, 2068–2093.

75 Z. Arcís-Castillo, F. J. Muñoz-Lara, M. C. Muñoz, D. Aravena, A. B. Gaspar, J. F. Sánchez-Royo, E. Ruiz, M. Ohba, R. Matsuda, S. Kitagawa and J. A. Real, *Inorg. Chem.*, 2013, **52**, 12777–12783.

76 T. Romero-Morcillo, N. De La Pinta, L. M. Callejo, L. Piñeiro-Lõpez, M. C. Muñoz, G. Madariaga, S. Ferrer, T. Breczewski, R. Cortés and J. A. Real, *Chem. - A Eur. J.*, 2015, **21**, 12112–12120.

77 S. M. Neville, G. J. Halder, K. W. Chapman, M. B. Duriska, B. Moubaraki, K. S. Murray and C. J. Kepert, *J. Am. Chem. Soc.*, 2009, **131**, 12106–12108.

78 D. Aravena, Z. A. Castillo, M. C. Muñoz, A. B. Gaspar, K. Yoneda, R. Ohtani, A. Mishima, S. Kitagawa, M. Ohba, J. A. Real and E. Ruiz, *Chem. - A Eur. J.*, 2014, **20**, 12864–12873.

79 J. A. Rodríguez-Velamazán, M. A. González, J. A. Real, M. Castro, M. C. Muñoz, A. B. Gaspar, R. Ohtani, M. Ohba, K. Yoneda, Y. Hijikata, N. Yanai, M. Mizuno, H. Ando and S. Kitagawa, *J. Am. Chem. Soc.*, 2012, **134**, 5083–5089.

80 F. J. Muñoz Lara, A. B. Gaspar, D. Aravena, E. Ruiz, M. C. Muñoz, M. Ohba, R. Ohtani, S. Kitagawa and J. A. Real, *Chem. Commun.*, 2012, **48**, 4686–4648.

81 P. D. Southon, L. Liu, E. A. Fellows, D. J. Price, G. J. Halder, K. W. Chapman, B. Moubaraki, K. S. Murray, J. F. L??tard and C. J. Kepert, *J. Am. Chem. Soc.*, 2009, **131**, 10998–11009.

82 X. Bao, H. J. Shepherd, L. Salmon, G. Molnár, M. L. Tong and A. Bousseksou, *Angew. Chemie - Int. Ed.*, 2013, **52**, 1198–1202.

83 M. M. Deshmukh, M. Ohba, S. Kitagawa and S. Sakaki, *J. Am. Chem. Soc.*, 2013, **135**, 4840–4849.

84 V. Niel, J. Martinez-Agudo and M. Munoz, *Inorg. Chem.*, 2001, **4144**, 3838–3839.

85 R. A. Bilbeisi, S. Zarra, H. L. C. Feltham, G. N. L. Jameson, J. K. Clegg, S. Brooker and J. R. Nitschke, *Chem. - A Eur. J.*, 2013, **19**, 8058–8062.

86 G. Lemercier, N. Bréfuel, S. Shova, J. a. Wolny, F. Dahan, M. Verelst, H. Paulsen, A. X. Trautwein and J. P. Tuchagues, *Chem. - A Eur. J.*, 2006, **12**, 7421–7432.

87 M. Sorai, J. Ensling, K. M. Hasselbach and P. Gutlich, *Chem. Phys.*, 1977, **20**, 197–208.

88 F. Neese and D. a Pantazis, *Faraday Discuss.*, 2011, **148**, 229–238; discussion 299–314.

89 S. Gómez-Coca, A. Urtizberea, E. Cremades, P. J. Alonso, A. Camón, E. Ruiz and F. Luis, *Nat. Commun.*, 2014, **5**, 4300.

90 E. Colacio, J. Ruiz, E. Ruiz, E. Cremades, J. Krzystek, S. Carretta, J. Cano, T. Guidi, W. Wernsdorfer and E. K. Brechin, *Angew. Chemie Int. Ed.*, 2013, **52**, 9130–9134.

91 J. Vallejo, I. Castro, R. Ruiz-Garcia, J. Cano, M. Julve, F. Lloret, G. De Munno, W. Wernsdorfer and E. Pardo, *J. Am. Chem. Soc.*, 2012, **134**, 15704–15707.

92 R. Herchel, L. Váhovská, I. Potocnak and Z. Trávnícek, *Inorg. Chem.*, 2014, **53**, 5896–5898.

93 D. Wu, X. Zhang, P. Huang, W. Huang, M. Ruan and Z. W. Ouyang, 2013, 1–7.

94 D. Gatteschi, R. Sessoli and J. Villain, *Molecular Nanomagnets*, Oxford University Press, 2006.

95 S. Gomez-Coca, E. Cremades, N. Aliaga-Alcalde and E. Ruiz, *J. Am. Chem. Soc.*, 2013, **135**, 7010–7018.

96 J. Tang and P. Zhang, in *Lanthanide Single Molecule Magnets*, Springer Berlin Heidelberg, Berlin, Heidelberg, 2015, pp. 41–90.

97 G. A. Craig and M. Murrie, *Chem. Soc. Rev.*, 2015, **44**, 2135–2147.

98 J. Hardy and F. Schacher, Eds., *Functional Metallosupramolecular Materials*, Royal Society of Chemistry, Cambridge, 2015.

99 A. F. Williams, C. Piguet and G. Bernardinelli, *Angew. Chemie Int. Ed. English*, 1991, **30**, 1490–1492.

100 M. Albrecht, *Chem. Rev.*, 2001, **101**, 3457–3498.

101 M. J. Hannon and L. J. Childs, *Supramol. Chem.*, 2004, **16**, 7–22.

102 S. Goetz and P. E. Kruger, *Dalton Trans.*, 2006, 1277–1284.

103 G. Maayan and M. Albrecht, Eds., *Metallofoldamers: Supramolecular Architectures from Helicates to Biomimetics*, John Wiley & Sons, 1st edn., 2013.

104 M. Albrecht, *Top. Curr. Chem.*, 2005, **248**, 105–139.

105 C. Piguet, G. Bernardinelli and G. Hopfgartner, *Chem. Rev.*, 1997, **97**, 2005–2062.

106 F. Cui, S. Li, C. Jia, J. S. Mathieson, L. Cronin, X. Yang and B. Wu, *Inorg. Chem.*, 2012, **51**, 179–87.

107 M. J. Hannon, *Chem. Soc. Rev.*, 2007, **36**, 280–295.

108 M. J. Prieto, E. Moldrheim, E. Sletten, I. Meistermann, C. J. Isaac, K. J. Sanders and A. Rodger, *Angew. Chemie - Int. Ed.*, 2001, **40**, 879–884.

109 L. Cerasino, M. J. Hannon and E. Sletten, *Inorg. Chem.*, 2007, **46**, 6245–6251.

110 A. Oleksi, A. G. Blanco, R. Boer, I. Usón, J. Aymamí, A. Rodger, M. J. Hannon and M. Coll, *Angew. Chemie - Int. Ed.*, 2006, **45**, 1227–1231.

111 G. N. Newton, T. Onuki, T. Shiga, M. Noguchi, T. Matsumoto, J. S. Mathieson,

M. Nihei, M. Nakano, L. Cronin and H. Oshio, *Angew. Chemie - Int. Ed.*, 2011, **50**, 4844–4848.

112 T. Shiga, M. Noguchi, H. Sato, T. Matsumoto, G. N. Newton and H. Oshio, *Dalton Trans.*, 2013, **42**, 16185–93.

113 C. S. Hawes, C. M. Fitchett and P. E. Kruger, *Supramol. Chem.*, 2012, **24**, 553–562.

114 M. D. Ward, *Org. Nanostructures*, 2008, 223–250.

115 W. Cullen, C. A. Hunter and M. D. Ward, *Inorg. Chem.*, 2015, **54**, 2626–2637.